

ABSTRACT

CHIKATIMARLA, SAI KIRAN. Numerical Analysis of Tesla Turbines. (Under the direction of Dr. James Braun).

Bladeless turbines are emerging as a promising solution for small-scale power extraction and hold great potential for enhancing energy efficiency in refrigeration cycles. This thesis explores the application of Tesla bladeless turbines as an alternative to traditional expansion valves, aiming to improve the coefficient of performance (COP) of refrigeration systems. Numerical analysis of these turbines was conducted using Computational Fluid Dynamics (CFD), employing an unstructured meshing approach with detailed refinement around the nozzle region. A comprehensive mesh sensitivity and convergence study ensured simulation accuracy and reliability.

Key performance parameters, including torque, power, and coefficient of discharge, were evaluated across various operating conditions, such as reduced mass flows and rotational speeds. Turbine characteristics, such as the relationship between total pressure ratio and specific power, were analyzed to identify the optimal operational range for the turbines. The research also examined the effects of nozzle shapes, inclination angles, and numbers to optimize turbine performance and maximize power output. Experimental validation was carried out using a physical prototype to compare the experimental data with the CFD model, reinforcing the accuracy of the numerical framework.

This study highlights the potential of Tesla turbines to enhance energy recovery in refrigeration cycles and provides critical insights into their design and optimization, paving the way for their integration into sustainable energy applications.

© Copyright 2024 by Sai Kiran Chikatimarla

All Rights Reserved

Numerical and Experimental Analysis of Tesla Turbines for Refrigeration Cycles

by

Sai Kiran Chikatimarla

A thesis submitted to the Graduate Faculty of
North Carolina State University
in partial fulfillment of the
requirements for the degree of
Master of Science

Mechanical Engineering

Raleigh, North Carolina
2024

APPROVED BY:

Dr. James Braun
Committee Chair

Dr. Sajjad Bigham

Dr. Andre Mazzoleni

DEDICATION

Dedicated to my parents and grandparents, for their unwavering love and sacrifices that shaped my journey, and to my friends, whose encouragement and support kept me motivated through every challenge.

BIOGRAPHY

Sai Kiran Chikatimarla was born on 1st October 1999 to Saritha and Mahesh Babu in India. He completed his undergraduate degree in Mechanical Engineering from Osmania University, Hyderabad in 2021. Before his masters, he delved into the corporate world, gaining industrial experience at Robert Bosch. As a Research Assistant at the BEFAST lab in the Department of Mechanical and Aerospace Engineering, he worked on the optimization of a Tesla Turbine using Numerical Analysis.

ACKNOWLEDGMENTS

The author owes his deepest gratitude to his advisor, Dr. James Braun, for being the cornerstone of this thesis and a constant source of encouragement and guidance throughout its development. He would like to thank NCSU MAE Senior design shop for letting him perform experiments in their workshop, NCSU HPC Cluster for the computational resources and Bernard Killingbeck from Tree Associates for the technical discussions and for providing the prototype of the Tesla Turbine. The author would also like to thank lab mates Jack Grunenwald, Liam Stumbar, Will Stigliano, and Eduardo Leite de Moraes for their time and advice.

TABLE OF CONTENTS

LIST OF TABLES	vii
LIST OF FIGURES	viii
NOMENCLATURE.....	xii
Chapter 1 Introduction.....	1
1.1 Tesla Turbine	1
1.1.1 Tesla Turbine Operation.....	2
1.1.2 Boundary Layer	3
1.1.3 Velocity Triangles	5
1.1.4 Unique Characteristics.....	7
1.1.5 Advantages and Disadvantages	8
1.1.6 Fundamental Equations	8
1.2 Literature review.....	11
1.2.1 Tesla Blood Pump	12
1.2.2 Tesla Turbine for ORC Applications.....	13
1.2.3 Tesla Heatsink	14
1.2.4 Small Scale Distributed Power Generation	15
1.2.5 Tesla Turboexpanders.....	16
1.3 Objectives	18
1.4 Methodology	19
1.5 Thesis Outline	20
Chapter 2 Baseline Numerical Analysis of Tesla Turbine	22
2.1 Numerical Modeling	22
2.1.1 Fluid domain.....	22
2.1.2 Mesh Sensitivity Study.....	23
2.1.3 Numerical Setup	25
2.2 Baseline CFD Results	27
2.2.1 Flowpath	28
2.2.2 Performance Characteristics	30
2.2.3 Reynolds Number	32
2.2.4 Laminar vs. Turbulent	34
2.2.5 Relative Flow Angle.....	35
2.2.6 Boundary layer	35
2.2.7 Turbine Characteristics.....	36

Chapter 3 Nozzle Optimization	38
3.1 Nozzle Contour Variation	38
3.2 Nozzle Inclination Variation	42
3.3 Multi Nozzle	47
Chapter 4 Experiment	50
4.1 Experimental set-up	50
4.1.1 Smaller Generator Test	51
4.1.2 Bigger Generator Test	53
4.2 CFD Validation	56
Chapter 5 Conclusions.....	58
REFERENCES.....	60

LIST OF TABLES

Table 2.1: Mesh Sensitivity Study	24
Table 3.1: Coefficient of Discharge.....	38
Table 4.1: Experiment-1 Results.....	52
Table 4.2: Experiment-2 Results.....	55

LIST OF FIGURES

Figure.1.1 Tesla's Patents: Turbine (left) and Fluid Propulsion (right)	1
Figure 1.2 Tesla Turbine Schematic (Copyright of Romanin [3]).....	2
Figure 1.3 Tesla Compressor (Copyright of Tiwari et al. [4]).....	3
Figure 1.4 Boundary layer development between two plates (Copyright of Cengel & Cimbala [5]).....	4
Figure 1.5 Flow in bladed turbine and compressor (left).....	5
Figure 1.6 Velocity triangles for Tesla rotor (Copyright of Renuke et al. [6]).....	7
Figure 1.7 Cross sectional schematic drawing of the motor and pump design (left), tesla blood pump (right) (Copyright of Izraelev et al. [30]	13
Figure 1.8 Tesla Turbine for ORC Applications (Copyright of Talluri et al. [32]).....	14
Figure 1.9 Tesla Heatsink (Copyright of et al. [33]).....	15
Figure 1.10 Tesla Turbine for Small Scale Power Generation (Copyright of Patel et al. [34]) ...	16
Figure 1.11 Refrigeration Cycle with an Expansion valve (left) vs. Turboexpander (right).....	17
Figure 1.12 Tree's Tesla Turbine in a Refrigeration Cycle.....	17
Figure 2.1 Tesla Turbine without housing	23
Figure 2.2 Simplified CAD two disks (left), Half of fluid domain between two disks (right) ...	23
Figure 2.3 Mass Flow Convergence	25
Figure 2.4 Mesh refinement and boundary conditions	26
Figure 2.5 Angular velocity contour of the stator-rotor case with a rotational speed of 5000 RPM 26	
Figure 2.6 Streamlines (top), Contours of Radial Velocity (middle) and Tangential Velocity (bottom) in simulations of half disk (left) vs. full disk (right).....	27

Figure 2.7 Static Pressure streamlines on disks at inlet stagnation pressure of 2 bar and rotational speed of 0 RPM (left) 5000 RPM (right)	28
Figure 2.8 Static Pressure streamlines on the disk at zero rotational speed and inlet stagnation pressure of 2 bar (top), 5 bar (middle), 8 bar (bottom).....	29
Figure 2.9 Static Pressure on the disk wall at inlet stagnation pressures of 2bar (top), 5bar (middle), 8bar (bottom).....	30
Figure 2.10 RPM (X) vs. (Y) mass flow rate (top), Torque (middle), Power (bottom) at various inlet stagnation pressures and disk RPMs.	32
Figure 2.11 Reynolds Number contour at the midpoint between two disks at an inlet pressure of 2 bar and 0 RPM.....	32
Figure 2.12 Reynolds Number contour at the midpoint between two disks at 0 RPM and inlet pressue of 5 bar (top) and 8 bar (bottom)	33
Figure 2.13 RPM (X) vs (Y) mass flow (top) and torque (bottom) for laminar and turbulent flows	34
Figure 2.14 Velocity triangle at rotor inlet (left), Power vs. Reactive flow angle at different inlet stagnation pressures (right)	35
Figure 2.15 Axial Velocity profile of fluid in the nozzle (left) Boundary layer on left side of the nozzle (right)	36
Figure 2.16 mass flow parameter (X) vs. total pressure ratio(left), specific power at various inlet stagnation pressures and disk RPMs (right)	37
Figure 3.1 Mach contour of the fluid on slot between upstream nozzle and disk at inlet stagnation pressures of 2bar	39

Figure 3.2 Mach contour of the fluid on slot between upstream nozzle and disk at inlet stagnation pressures of 5bar (left), 8bar (right)	40
Figure 3.3 Total Pressure contour on the slot between upstream nozzle and disk for flat (left) and CD (convergent divergent) (right) configurations with an inlet stagnation pressure of 2 bar	40
Figure 3.4 Coefficient of discharge (X) vs. RPM (Y)	41
Figure 3.5 Total pressure (left), Ratio of total pressure loss to inlet total pressure (right) from Station 1 to Station 4	41
Figure 3.6 Geometry of the nozzle slot with a 15° inclination between the upstream nozzle and disk.....	42
Figure 3.7 Comparison of geometries at inclination of 45 (top) and 50 degrees (bottom).....	43
Figure 3.8 Mass flow rate (Y) vs. RPM (X) at different nozzle inclinations	44
Figure 3.9 RPM (X) vs. (Y) Torque (top), Power (bottom) at different nozzle inclinations.....	45
Figure 3.10 Mach contour of the fluid for the 35-degree inclination at 0 RPM (left) and 5000 RPM (right)	45
Figure 3.11 Mach contours of the fluid at the nozzle slot for inclination angles of 15 (top), 50 (middle), and 75 (bottom) degrees	46
Figure 3.12 Torque (left y-axis) and Power (right y-axis) vs. Nozzle inclinations (X), given a mass flow inlet of 7E-5 kg/s per nozzle.....	47
Figure 3.13 Fluid domain between two disks for the configuration with 2 (left) and 4 (right) nozzles	48
Figure 3.14 Mass flow rate (X) vs. Power (Y)	49
Figure 4.1 Experimental setup 1 of Mark-1	51

Figure 4.2 Power (Y) vs RPM (X) for Experiment -1 52

Figure 4.3 Experimental setup 2 of Mark-1 53

Figure 4.4 Pressure (X) vs. (Y) Current (top) and Voltage (bottom) for Experiment-2..... 54

Figure 4.5 Current (Y) vs. Speed (X) for Experiment - 2..... 56

Figure 4.6 Power (Y) vs. Pressure (X) for Experiment and CFD (laminar and turbulent)..... 57

NOMENCLATURE

τ	Shear Stress, (N/m^2)	ε	Expansion ratio
μ	Dynamic Viscosity (Pa.s)	$p_{in.tot}$	Total Pressure at the inlet, (N/m^2)
ρ	Density , (kg/m^3)	$p_{e.st}$	Static Pressure at the exit, (N/m^2)
p	Pressure, (N/m^2)	P_t	Total Pressure, (N/m^2)
v	Velocity, (m/s)	T_t	Total Temperature (K)
$k,$	Specific heat ratio	R	Gas constant (J/kg.K)
T	Temperature (K)	$T_{in.tot}$	total temperature at the inlet
l	Gap between disks (m)	C_p	Specific heat at constant pressure (J/kg.K)
Re	Reynolds Number	\dot{m}	Mass flow rate (kg/s)
e_u	Specific energy (J/kg)		
τ_o	Torque (Nm)		
r_o	Outer radius (m)		
v_{to}	Tangential Velocity of outer disk (m/s)		
r_i	Inner radius (m)		
v_{ti}	Tangential Velocity of inner disk (m/s)		
P_{CFD}	Power from CFD (Watts)		
η_{CFD}	Efficiency		
ω	Rotational velocity (rad/s)		

CHAPTER 1

Introduction

1.1 Tesla Turbine

The Tesla Turbine, also known as the Bladeless Turbine, is a unique turbomachinery design invented by Nikola Tesla in the early 1910s. Tesla patented this invention in 1913 [1-2], as shown in Figure.1.1, considering it one of his most important contributions to engineering. Unlike conventional turbines that use blades, the Tesla Turbine operates on the principle of the boundary layer effect, utilizing fluid properties such as adhesion and viscosity. He initially developed this turbine while working on a lightweight engine for his envisioned "flying machine". He demonstrated a small device capable of generating 110 horsepower, showcasing its potential for high power-to-weight ratios. Regarding efficiency and performance, Tesla claimed potential efficiencies of up to 95%. However, practical implementations have typically achieved lower efficiencies, often around 40%.

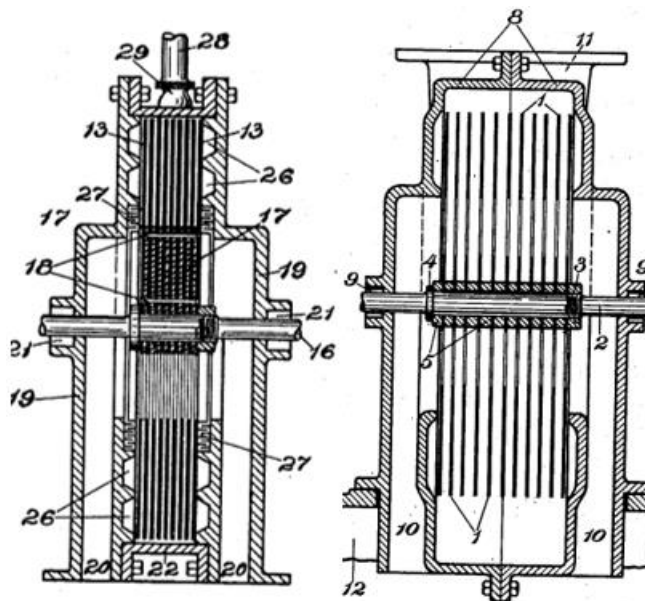


Figure.1.1 Tesla's Patents: Turbine (left) and Fluid Propulsion (right)

The key components of a Tesla Turbine include:

- Rotor Assembly: Multiple smooth, closely spaced disks mounted on a shaft
- Stator: A cylindrical housing encasing the rotor assembly
- Inlet Nozzles: Direct the working fluid tangentially between the disks
- Central Exhaust Ports: Allow fluid exit after spiraling towards the center

1.1.1 Tesla Turbine Operation

Figure 1.2 shows the schematic of a tesla turbine. It consists of multiple disks parallelly mounted on a shaft with spacing between them. The fluid enters tangentially to the disks (rotor), follows a spiral path on the disk and leaves through the center axially.

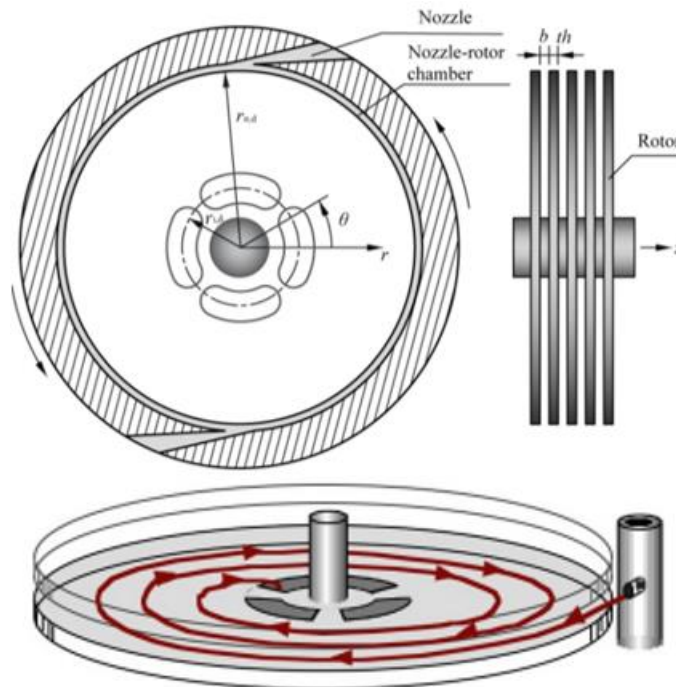


Figure 1.2 Tesla Turbine Schematic (Copyright of Romanin [3])

A tesla turbine can also act as a compressor as shown in Figure 1.3 by the reversal of flow direction i.e., fluid enters from the central holes of the disks and leaves through the periphery. The relative velocity between the fluid and disks of this is very less compared to conventional bladed turbines. The flow inside the rotor is laminar due to lower relative velocity. This is the key factor for efficient energy transfer between fluid and disk. The energy exchange is due to the shear forces

between disks and fluid. The drag generated from the shear forces will be in the direction of the disk's rotation. Hence, in the case of this turbine, viscous shear drag is in favor of power generation unlike conventional bladed turbines.

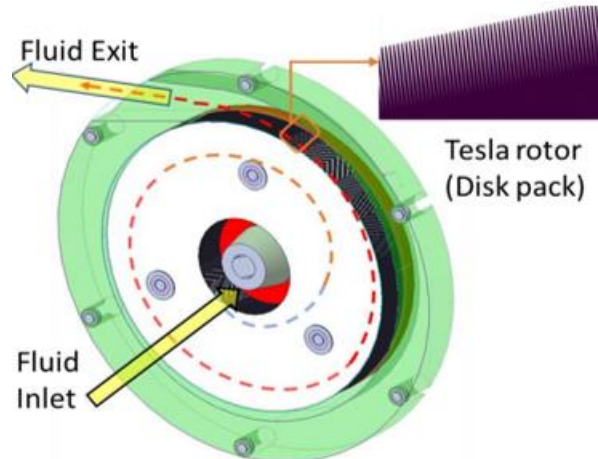


Figure 1.3 Tesla Compressor (Copyright of Tiwari et al. [4])

1.1.2 Boundary Layer

Boundary layers form between the two disks as shown in Figure 1.4 when the fluids flow between them. Thus, generating the shear stress on the wall. This shear stress has two components, tangential and radial. The tangential one is responsible for the torque on the rotor while the radial component merely contributes to the viscous frictional loss. Shear stress on the wall is given by

$$\tau = \mu \frac{du}{dy} \quad (1)$$

In bladed turbomachinery, friction acts as a hindrance to performance, whereas in bladeless turbomachinery, such as Tesla turbines, it aids in momentum transfer. In conventional bladed systems, viscosity-induced friction leads to energy losses and impacts overall efficiency. This occurs because friction generates shear forces aligned with the fluid flow direction. In the stator, this friction remains in the working fluid, increasing its entropy. In the rotor, shear forces not only

increase fluid entropy but also reduce the net power produced or consumed at the rotating shaft due to their opposition to blade tangential speed.

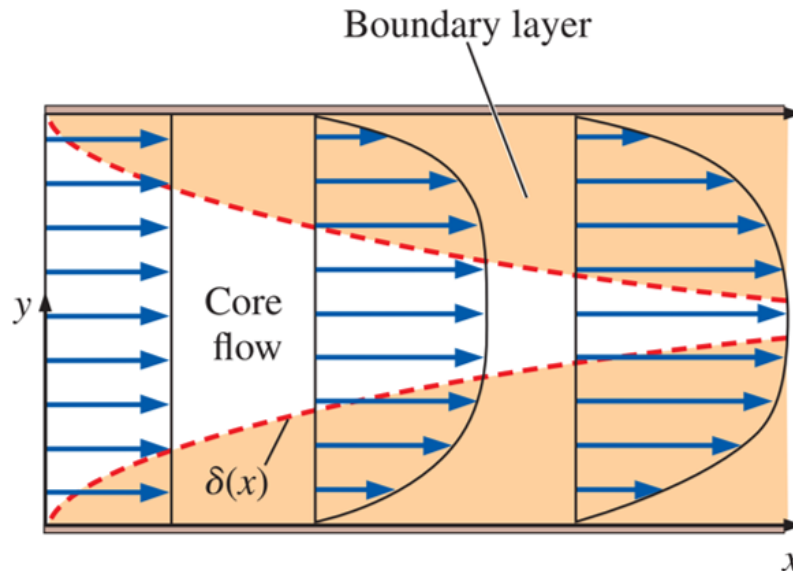


Figure 1.4 Boundary layer development between two plates (Copyright of Cengel & Cimbala [5])

Figure 1.5 (left) shows the flow directions in traditional bladed turbines and compressors, shear forces parallel to flow velocity vectors result in friction work that is not captured by the rotor, thus remaining in the fluid and causing an entropy increase. Conversely, in a Tesla turbine, flow direction shown in Figure 1.5 (right), where the rotor is bladeless, the tangential component of friction forces aligns with the rotor's tangential speed. This unique configuration allows drag to perform work collected by the rotor rather than being left in the working fluid. Consequently, this friction work does not increase entropy because it is extracted by the rotor like regular mechanical work.

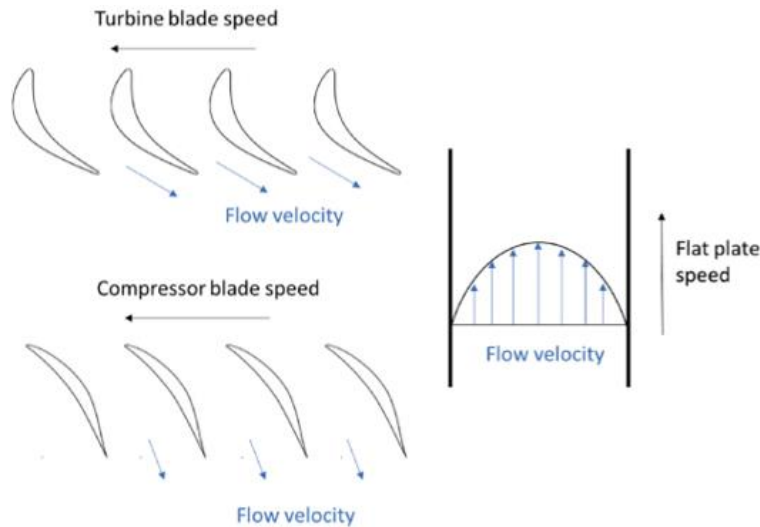


Figure 1.5 Flow in bladed turbine and compressor (left) flow between two disks in a bladeless turbine (right) (Copyright of Renuke et al. [6])

1.1.3 Velocity Triangles

Velocity triangles are a graphical representation used to analyze the velocities of fluids as they interact with turbine blades or discs. These triangles help understand the relationship between the absolute velocity of the fluid, the relative velocity with respect to the moving parts of the turbine, and the rotor's tangential velocity. In traditional bladed turbines, these triangles are crucial for designing and optimizing blade angles and rotor speeds to maximize efficiency.

In Tesla turbines, which are bladeless, the concept of velocity triangles is adapted to account for the unique flow dynamics between smooth discs. The fluid enters tangentially at high speed from the outer edge and spirals inward toward the center exhaust, transferring momentum to the discs through viscous drag rather than direct impact. The velocity triangle in a Tesla turbine involves analyzing the inlet and exit velocities of the fluid relative to the disc speed. The inlet velocity triangle considers parameters like the inlet flow angle and velocity ratio, which affect how efficiently energy is transferred to the discs. At the exit, if the tangential velocity of the fluid is

higher than that of the disc tip, it results in positive torque but also potential energy loss if not properly managed.

Figure 1.6 which is directly taken from the Tesla Turbine book authored by Renuke et.al. shows the velocity triangles at the inlet and exit of Tesla rotor. For optimal performance in Tesla turbines, the fluid should ideally enter the rotor from the stator in a nearly tangential direction. However, achieving this precise alignment is challenging due to design constraints. Consequently, researchers have often employed stators with a positive flow angle greater than 5° for practical manufacturing reasons. The velocity triangles at the inlet and exit of the Tesla rotor illustrate these dynamics, with flow angles measured relative to the tangential direction along the disk tip velocity vector. The angle between the absolute velocity vector and the tangential direction is known as the inlet flow angle, while the angle between the relative velocity vector and the tangential direction is referred to as the relative flow angle.

Two scenarios are depicted based on the inlet velocity ratio, which is the ratio of inlet tangential velocity to disk tip velocity. In Case 1-3, where this ratio exceeds 1, the inlet tangential fluid velocity is greater than the disk tip speed. This results in a positive relative velocity that generates shear forces on the disks, producing torque. However, energy can be lost at the exit if not properly managed, as excess tangential fluid velocity does not contribute to work exchange with the disk. In Case 2-4, where the ratio is less than 1, flow reversal occurs, leading to inefficient energy transfer and increased losses due to frictional viscous forces acting in opposition to disk rotation. To maximize efficiency, it is crucial to minimize the inlet flow angle and ensure that the inlet velocity ratio remains above 1.

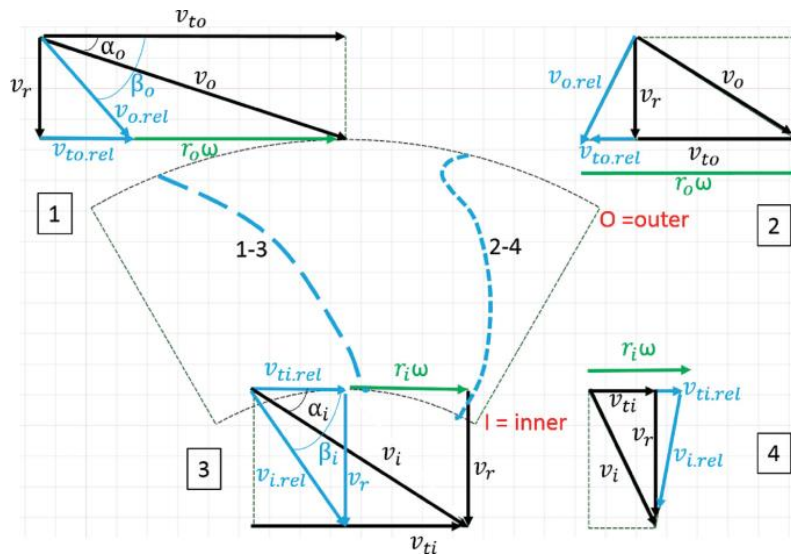


Figure 1.6 Velocity triangles for Tesla rotor (Copyright of Renuke et al. [6])

1.1.4 Unique Characteristics

Some unique characteristics of the Tesla Turbine include:

- High-Speed, Low-Torque operation
- Simple design compared to conventional turbines
- Versatility in operating with various fluids, including particle-laden or abrasive substances

The turbine's performance is highly dependent on factors such as disk spacing, fluid properties, and inlet/outlet design. Despite not achieving widespread commercial success in its early days, the Tesla Turbine concept has seen renewed interest in recent years, with potential applications in:

- Microfluidics
- Renewable Energy (geothermal power generation and industrial waste heat recovery)
- Pumps and Compressors
- Medical Devices (possible use in blood pumps)
- Advantages of the Tesla Turbine include:
 - Simple and cost-effective construction

- Ability to handle various fluids, including those with particles or high viscosity
- Potential for high efficiency in certain applications

1.1.5 Advantages and Disadvantages

Some of the main advantages and disadvantages of the Tesla Turbines as mentioned by Renuke in his Tesla Turbine book are:

Advantages:

- High rotor efficiency
- Reversible Machine
- Absence of impingement (erosion free)
- Laminar flow inside the rotor, which leads to very low vibrations
- High reliability
- Easy to manufacture and maintain
- Ability to handle dirty fluids like abrasive fluids, two-phase fluids, etc.

Disadvantages:

- Large gap between theoretical and experimental performance
- No detailed research on stators suitable for bladeless turbomachinery
- No systematic assessment of losses
- Very few experimental data available for complete turbomachinery set-ups.

1.1.6 Fundamental Equations

The computational fluid dynamics (CFD) analysis of Tesla turbines involves solving a set of fundamental equations that govern fluid flow behavior. These equations are primarily derived from the Navier-Stokes (NS) equations, which describe how the velocity, pressure, density, and temperature of a moving fluid interact over time and space. In the analysis of Tesla

turbines, these equations allow for a detailed examination of flow characteristics, turbulence, and efficiency under varying operational conditions.

Equation (2) stands for mass conservation, or continuity equation, it ensures mass conservation by stating that the rate of change of density within a control volume, plus the net flux of mass out of that volume, must be zero. In CFD simulations of Tesla turbines, this equation helps track how fluid density changes as it moves through the rotor and stator.

$$\frac{\delta\rho}{\delta t} + \nabla \cdot (\rho\bar{v}) = 0 \quad (2)$$

Equation (3) is the general form of the Navier-Stokes equation for momentum conservation. It describes how momentum is transferred within a fluid due to pressure gradients and viscous stresses. The term τ represents the viscous stress tensor, which accounts for internal friction due to fluid viscosity.

$$\frac{\delta(\rho\bar{v})}{\delta t} + \nabla \cdot (\rho\bar{v}\bar{v}) = -\nabla p + \nabla \cdot (\bar{\tau}) \quad (3)$$

The stress tensor τ models how shear stresses arise in a viscous fluid. In Tesla turbines, where boundary layers play a significant role, this term is critical for capturing how viscous forces influence fluid motion between closely spaced disks.

$$\bar{\tau} = \mu \left[(\nabla\bar{v} + \nabla\bar{v}^T) - \frac{2}{3}\nabla \cdot \bar{v}\bar{I} \right] \quad (4)$$

Equation (5) stands for energy conservation; it accounts for internal energy, kinetic energy, heat conduction, and viscous forces work. In Tesla turbines, where heat transfer and viscous dissipation are key factors, this equation helps predict temperature distributions and energy losses.

$$\frac{\delta}{\delta t} \left[\rho \left(e_u + \frac{v^2}{2} \right) \right] + \nabla \cdot \left[\rho\bar{v} \left(e_h + \frac{v^2}{2} \right) \right] = \nabla \cdot (k\nabla T) + \nabla \cdot (-\rho\bar{v} + \bar{\tau} \cdot \bar{v}) \quad (5)$$

Reynolds number, which is calculated using the equation (6) is a dimensionless quantity that characterizes the flow regime (laminar vs. turbulent). In Tesla turbines, low Reynolds numbers are often encountered due to small gaps between disks and relatively low velocities. This results in laminar flow dominated by viscous effects.

$$Re = \frac{\rho \cdot l \cdot v}{\mu} \quad (6)$$

At low Reynolds numbers, viscous forces dominate over inertial forces. This simplified momentum equation (7) is used to model flow in Tesla turbines where viscosity plays a significant role in determining performance.

$$Re \frac{D\bar{v}}{Dt} = -\nabla p + \nabla^2 \bar{v} \quad (7)$$

The shear stress τ in a fluid flow is described by the equation (8), where μ is the dynamic viscosity, and du/dy is the velocity gradient perpendicular to the flow direction. This relationship is central in analyzing boundary layer effects on the turbine's disk surfaces, which influence flow drag and energy dissipation.

$$\tau = \mu \frac{du}{dy} \quad (8)$$

Torque can also be calculated using the Euler equation, which is given in equation (9), it quantifies the change in angular momentum of the fluid as it moves through the rotating system, where m is the mass flow rate, r_o and r_i are the outer and inner radial positions, and v_{to} and v_{ti} are the tangential velocities at these radii.

$$\tau_o = m \cdot (r_o v_{to} - r_i v_{ti}) \quad (9)$$

Once the torque is obtained from the CFD simulations, power can be calculated as product of torque and rotational velocity of disc in rad/s which is shown in equation (10).

$$P_{CFD} = \tau \omega \cdot \omega \quad (10)$$

And the efficiency, which is shown in equation (11), can be calculated as ratio of power obtained from CFD to the ideal power and the parameter ε represents the expansion ratio which is the ratio total pressure at inlet to static pressure at the exit.

$$\eta_{cfd.tot.st} = \frac{P_{CFD}}{\dot{m} C_p T_{in.tot} \left(1 - \frac{1}{\varepsilon^{\frac{k-1}{k}}} \right)} \quad (11)$$

$$\varepsilon = \frac{p_{in.tot}}{p_{e.st}} \quad (12)$$

1.2 Literature review

Tesla claimed it to have remarkably high rotor efficiency which was proved analytically. But the practical prototypes have isentropic efficiencies in the range of 20-40%. Investigation into the tesla turbines have been ongoing since the 1950s [7], [8].

Various aspects of two-phase flow are explored in references [9], [10], [11], [12], [13]. Research has been focused on improving the efficiency of the Tesla turbine. Guha and Smiley [14] investigated the inlet and nozzle losses and created an improved design of the nozzle, significantly enhancing the efficiency while achieving uniformity in the velocity profile of the jet. Guha and Sengupta [15] conducted numerical investigations to analyze the impact of nonuniform admission at the inlet of the Tesla rotor, the influence of a discrete number of nozzles, and considerations such as disk thickness and radial clearance between the stator and rotor. Research in the field of Tesla turbines till 1991 has been summarized by Rice [16]. Rice [8] carried out an analytical study of Tesla turbine rotor and experimented on some models using air as a working fluid and showed that high rotor efficiencies can be achieved at very low flowrate. Boyak and Rice [17] developed a 3D integral solution for the flow inside Tesla turbine. They validated this model with

experimental data, demonstrating its capability to accurately predict pressure distributions within the Tesla rotor. Similarly, Basset [18] developed a model using compressible flow and validated it with experimental data, defining optimum values for radius ratio and Reynolds number. Numerous dissertations offer detailed descriptions of various investigations into the flow dynamics and performance of Tesla disc turbines [3, 19-26]. Manfrida et al. incorporated convergent nozzle configurations for Organic Rankine cycles [27] and Okamoto et al. [28] experimentally explored the impact of nozzle angles on turbine performance. They employed two convergent nozzles with adjustable angles and varied the nozzle angle up to 5 degrees. Their findings showed the presence of an optimal nozzle angle for efficiency, with even slight deviations resulting in significant efficiency changes. Finally, Renuke [29] characterized various losses in the Tesla turbine to three sections: rotor, stator and the clearance between rotor and stator. This paper first details the numerical procedure to analyze an experimentally built Tesla turbine, followed by a discussion on the performance sweep across multiple pressure ratios and the effect of inflow angles on the performance. Some of the applications of the Tesla turbine are discussed in the following sub sections.

1.2.1 Tesla Blood Pump

Penn State University developed a continuous left ventricular device (LVAD) [30]. It is a device to replace the function of the human heart in patients with cardiac insufficiency. [31] describes the design and test results of the passively suspended Tesla type LAVD blood pump shown in Figure 1.7 Cross sectional schematic drawing of the motor and pump design (left), Tesla blood pump (right). The prototype device discussed in the study is a pump with a diameter of 50 mm and a length of 75 mm. It features a rotor with a density lower than that of blood, which creates a buoyant centering force when spinning inside the stator, suspending the rotor radially. Axial

magnetic forces between the rotor and stator maintain axial stability. The pump can deliver up to 10 liters per minute at an 8000 RPM speed, achieving a 70-mmHg head rise. It has demonstrated a low normalized index of hemolysis, below 0.02 mg/dL, for flow rates between 2 and 9.7 L/min. Additionally, an inlet pressure sensor is integrated into the inlet cannula wall for control purposes. Initial *in vivo* studies have shown promising results, indicating potential for further research and development in medical applications. The Tesla pump offers significant advantages over conventional pumps, primarily due to its bladeless design, which minimizes wear and tear, reduces mechanical failure risk, and enhances device longevity. Its non-contact operation significantly reduces hemolysis, making it ideal for medical applications involving blood handling. This innovative design improves efficiency and durability while ensuring safer fluid handling compared to traditional pumps.

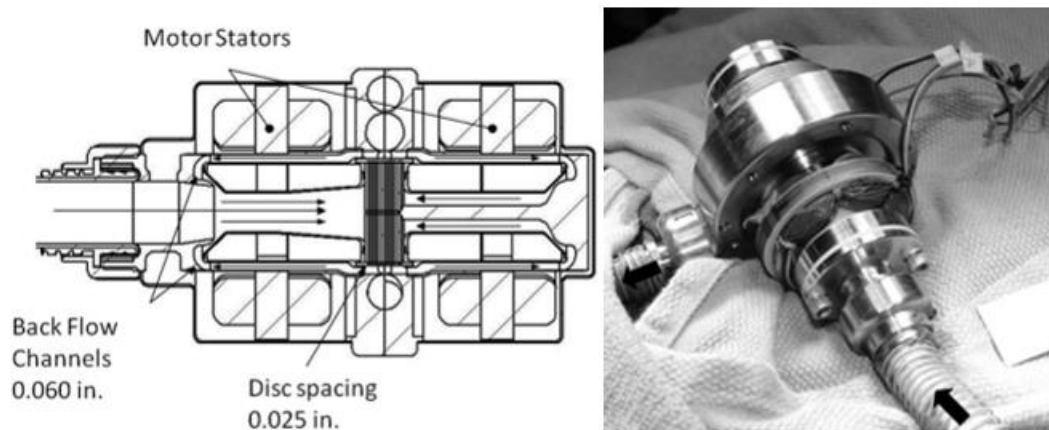


Figure 1.7 Cross sectional schematic drawing of the motor and pump design (left), tesla blood pump (right) (Copyright of Izraelev et al. [30])

1.2.2 Tesla Turbine for ORC Applications

Talluri's study [32] presents the Tesla turbine as a micro expander for Organic Rankine Cycle (ORC) applications, highlighting its suitability for small and micro-sized systems where

low-cost components are helpful for exploiting residual pressure drops. The study outlines a design procedure for the Tesla turbine tailored to ORC applications, involving thorough optimization by evaluating each component's losses and introducing an innovative rotor model. Three turbine configurations with varying expander sizes were assessed, achieving a total-to-static efficiency of 64% using N-hexane as the working fluid.

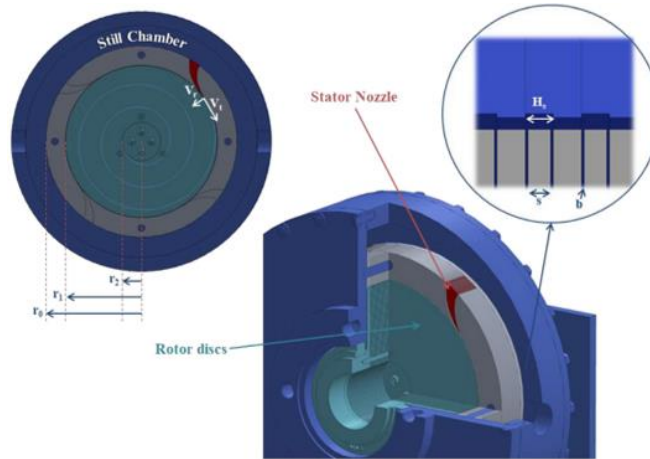


Figure 1.8 Tesla Turbine for ORC Applications (Copyright of Talluri et al. [32])

1.2.3 Tesla Heatsink

Ruiz's study [33] investigates the heat transfer and pressure drop characteristics of a high heat flux microchannel cooling system with spiraling radial inflow. This system is designed to enhance heat transfer through a simple inlet and outlet configuration while ensuring uniform flow distribution. Utilizing water as the working fluid, the system (Figure 1.9 *Tesla Heatsink*) features a microchannel with a 1 cm radius and a 300 μm gap height and is heated from a copper conducting wall. The experimental results indicate that the system experiences, on average, a 76% larger pressure drop compared to an analytic model for laminar flow in parallel disk systems with spiral radial inflow. Notably, the mean heat transfer coefficients are up to four times greater than those for unidirectional laminar fully developed flow between parallel plates with the same gap height. Flow visualization studies reveal secondary flows and turbulence onset at higher flow rates, contributing to enhanced heat transfer coefficients. Additionally, the system maintains small

thermal gradients on the surface, with an average surface temperature variation of 18% of the total bulk fluid temperature gain. This cooling system demonstrates promising potential for applications in electronics and concentrated photovoltaics, achieving a heat flux of 113 W/cm^2 at a surface temperature of 77°C with a pumping power to heat rate ratio of 0.03%.

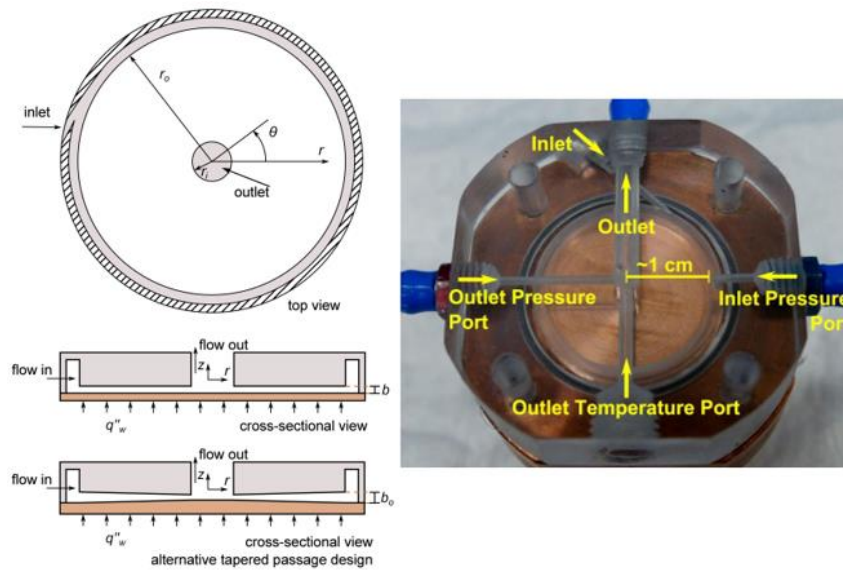


Figure 1.9 Tesla Heatsink (Copyright of et al. [33])

1.2.4 Small Scale Distributed Power Generation

Patel et al. [34] demonstrated the use of a Tesla turbine for direct conversion of biomass into small-scale distributed power generation. Featuring a specially designed multiple-disk rotor as shown in Figure.1.1, operates under skin friction drag from hot gas flow between parallel plates. Known for its resistance to erosion, it can handle particle-laden gases and ash-containing biomass fuels. In experiments, wood-derived sawdust and natural oats were used as test fuels, injected into a stream of vitiated hot air for complete combustion. The study assessed deposition, erosion, and corrosion effects on the BLT components over 40 hours of operation, consuming 68 kg of biomass. Initial firing used 10% biomass, increasing to 100%, achieving isentropic turbine efficiencies of 11% at 3.2 kW and 6284 rpm. No significant component degradation was observed, with only minor soot deposition. The study highlights the potential for cost-effective electricity production

from biomass in distributed-generation applications, though improvements in isentropic efficiency are needed to reach meaningful overall cycle efficiency.

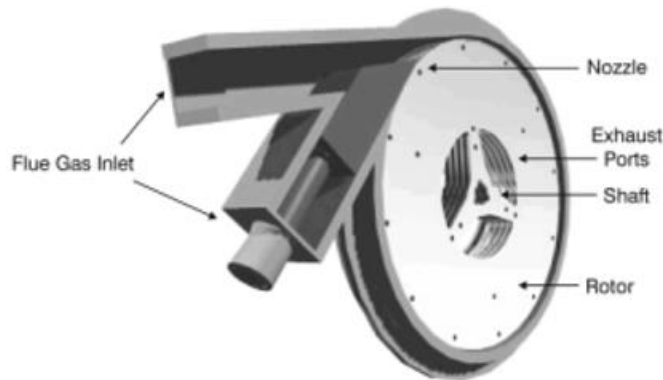


Figure 1.10 Tesla Turbine for Small Scale Power Generation (Copyright of Patel et al. [34])

The Tesla Turbine remains an intriguing concept in fluid mechanics and energy conversion. While it has not yet displaced conventional turbine designs in most applications, ongoing research continues to explore its potential in niche areas where its unique characteristics can be advantageous.

1.2.5 Tesla Turboexpanders

Passalacqua et al. [35] explored the integration of Tesla turboexpanders within CO₂ refrigeration cycles, emphasizing their potential for enhancing thermodynamic performance and economic viability. The study compared various cycle layouts, including those with traditional lamination valves, ejectors, and Tesla expanders. Figure 1.11 cycles with expansion valve (left) and turboexpander(right). Results demonstrated that Tesla expanders could improve the coefficient of performance (COP) by 8% to 22%, depending on the cycle configuration and cold-source temperature. Additionally, the use of Tesla turboexpanders resulted in lower specific costs compared to conventional layouts. This research highlights the advantages of Tesla expanders in small-scale energy systems, particularly due to their high rotor efficiency and low sensitivity to downscaling effects, making them suitable for sustainable energy applications.

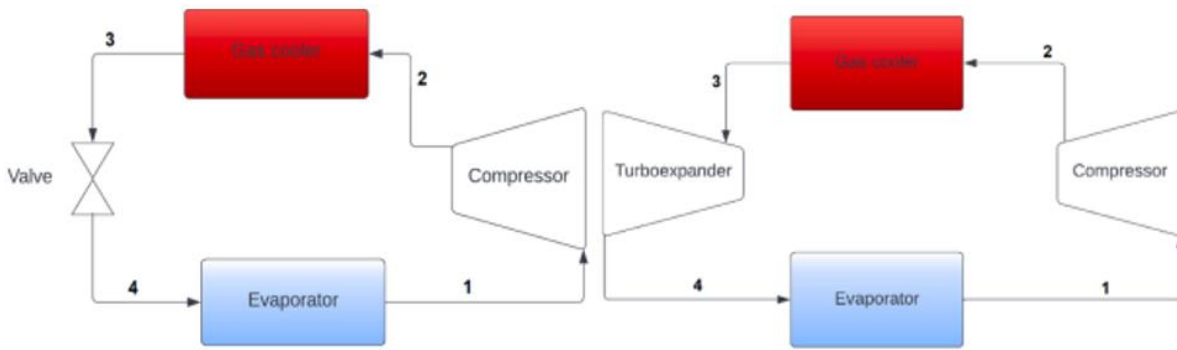


Figure 1.11 Refrigeration Cycle with an Expansion valve (left) vs. Turboexpander (right)

This study focuses on one such Tesla turbine to be used in refrigeration cycles being developed by Tree Associates, an energy start-up based in the UK.

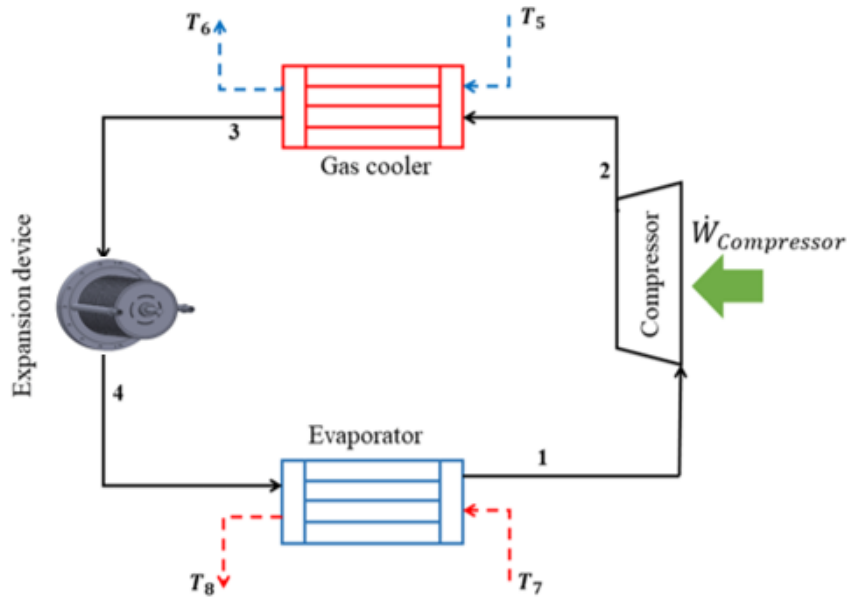


Figure 1.12 Tree's Tesla Turbine in a Refrigeration Cycle

Figure 1.12 shows a Tesla Turbine used in a refrigeration cycle as an expansion device instead of an expansion valve. Integrating a Tesla turbine into a refrigeration cycle offers a novel approach to enhancing the coefficient of performance (COP) by utilizing energy that is typically wasted during the expansion process. Traditionally, refrigerants in a cycle pass through an expansion valve where high-pressure fluid energy is dissipated as heat. By replacing the expansion valve with a Tesla turbine, this energy can be harnessed as the refrigerant expands across the

turbine's disk surfaces, converting some of the pressure energy into mechanical work. This recovered work can then be redirected to auxiliary functions, such as partially driving the compressor, effectively reducing the electrical load and, consequently, the system's overall power consumption. The impact on COP is significant because COP is directly proportional to the cooling effect per unit of work input; thus, any reduction in input power translates to improved performance. Additionally, by optimizing parameters such as nozzle configuration and flow angle within the Tesla turbine, the system can be tuned for maximum energy recovery, making it adaptable to different operating pressures and refrigerants. This energy-efficient integration not only boosts the refrigeration cycle's COP but also supports sustainable energy practices in thermal management applications.

1.3 Objectives

The objectives of this research focus on a comprehensive analysis of the Tesla turbine for application in refrigeration cycles through Computational Fluid Dynamics. A primary goal is to determine mass flow rates, torque, power output, and other performance metrics across various pressure ratios and rotational speeds. By establishing how these parameters vary with different operating conditions, this study will provide insights into the turbine's efficiency and performance. Additionally, adjustments to the turbine's design are considered to reduce losses, including exploring modifications to the nozzle contour. By changing the nozzle's shape from a flat to convergent-divergent configuration, this research aims to mitigate the mass flow losses i.e., to increase the coefficient of discharge as the mass flow is directly proportional to torque and enhance the turbine's overall performance, making it more efficient for refrigeration applications.

Further optimization objectives include identifying the ideal nozzle angle and determining the optimal number of nozzles, both of which significantly affect flow behavior and power

extraction. Experimental validation will be conducted to compare observed data with the CFD model's predictions, strengthening the accuracy of simulation results. To broaden the understanding of the turbine's behavior, turbine characteristics will be plotted which can be used to the turbine performance across different pressure ratios and with alternative working fluids. This approach aims to generate a robust dataset that can inform future design improvements, particularly for adapting the Tesla turbine's performance to varying industrial applications.

1.4 Methodology

This study involves a comprehensive numerical analysis of bladeless turbines using Computational Fluid Dynamics (CFD). The process begins with setting up the fluid domain, utilizing CAD model. The CAD models are refined using SolidWorks to clean up unnecessary details and create the fluid domain between two disks. Due to the symmetry of the design, only half of the domain is used in some simulations to reduce computational load.

The meshing of the fluid domain is performed using Hexpress, focusing on creating a high-quality mesh that captures intricate flow characteristics, particularly around the nozzle region. A mesh sensitivity study is conducted to ensure the accuracy and reliability of the simulation results. This study involves running simulations with varying mesh densities to achieve mesh independence, where further refinement does not significantly alter the results. This step is crucial for optimizing computational efficiency and ensuring that spatial discretization errors are minimized.

Simulations are executed using iCFD++, a robust CFD software, to evaluate turbine performance under various conditions with air as the working fluid. Post-processing of simulation data is carried out using MATLAB and Tecplot, allowing for detailed analysis of flow behavior,

energy transfer mechanisms, and performance parameters such as torque, power, and coefficient of discharge.

To validate the CFD results, an experimental setup was constructed. A generator was connected to the turbine, and tests were conducted by increasing load resistors connected to the generator and increasing the mass flow to the turbine. Power output was calculated as the product of voltage and current across the generator which were measured using the multimeters connected to it. Compressed air was passed into the turbine, with pressure monitored through a pressure meter at the inlet. A digital tachometer recorded the turbine's speed. Experiments were performed with two different motors of varying wattage capacities to assess performance across different operational conditions.

1.5 Thesis Outline

The thesis opens with an Introduction that outlines the background and motivation behind the study of bladeless turbines, clearly stating the objectives and scope of the research. This section also provides a structured overview of the thesis to guide the reader. A Literature Review follows, presenting a comprehensive overview of existing research on bladeless turbines, with a focus on previous studies in their design, performance, and applications of Computational Fluid Dynamics (CFD) in turbomachinery. This chapter also identifies key gaps in current research that this study seeks to address.

The Methodology chapter details the numerical setup, covering CAD model preparation, fluid domain definition, and considerations for computational efficiency through symmetry. The meshing process is described in depth, including the use of Hexpress for mesh generation and a sensitivity study to ensure mesh independence. Execution of simulations in iCFD++ is explained,

along with post-processing and data analysis techniques using MATLAB and Tecplot to evaluate performance metrics.

Chapter 2 presents the results for the tangential bladeless turbine, detailing the CFD model set up and simulation outcomes across various inlet stagnation pressures and rotor speeds. Key performance metrics, including mass flow, torque, and power output, are analyzed with a mesh sensitivity study confirming mesh independence at pressures of 2, 5, and 8 bar and rotor speeds up to 15,000 RPM. A comparative assessment with experimental data evaluates model accuracy, showing how different nozzle configurations, such as flat versus converging-diverging profiles, influence total pressure loss, discharge coefficient, and power output. The study also explores the impact of optimal nozzle inclination angles and the number of nozzles, identifying a favorable range for flow angles between 45 and 50 degrees to maximize power. Experimental validation is conducted using a generator setup with load resistors, measuring voltage, current, pressure, and speed, which further supports the CFD results and confirms performance trends under load, thereby reinforcing the model's accuracy and design insights for bladeless turbines in refrigeration cycles.

The thesis concludes with a Conclusion that summarizes major findings, discusses their implications for bladeless turbine design and energy efficiency in refrigeration cycles, and offers recommendations for future research. Finally, the References section and Appendices provide additional supporting data, detailed diagrams of experimental setups, and further analysis on nozzle and motor configurations, completing the comprehensive study of bladeless turbine applications in refrigeration.

CHAPTER 2

Baseline Numerical Analysis of a Tangential Bladeless Turbine

In the previous chapter's literature review, it was highlighted that incorporating a Tesla turbine as the expansion device in a refrigeration cycle can enhance the system's coefficient of performance (COP). Tree Associates, a UK-based startup, has been actively developing this Tesla turbine. To understand its potential in refrigeration applications, computational fluid dynamics (CFD) simulations were conducted, focusing on the turbine's internal fluid behavior and examining how key parameters respond to variations in pressure ratio and rotational speed (RPM). The CFD analysis sheds light on fluid dynamics, such as velocity profiles and torque generation, providing insights into optimizing the Tesla turbine for refrigeration cycles.

2.1 Numerical Modeling

2.1.1 Fluid domain

To streamline the process, the CAD model of the entire turbine assembly (as shown in Figure 2.1) was simplified to encompass only two disks, as illustrated in Figure 2.2 (left). Furthermore, the fluid domain is adjusted to solely feature a smooth disk, by removing all the intricate grooves and flow-guiding diamonds to reduce computational cost. Leveraging the periodic nature of flow patterns within the domain, the analysis focused on just half of the fluid region between the two disks, as depicted in Figure 2.2 (right)

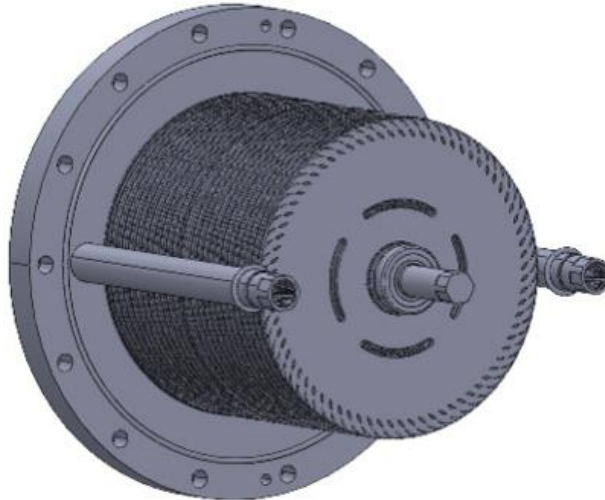


Figure 2.1 Tesla Turbine without housing

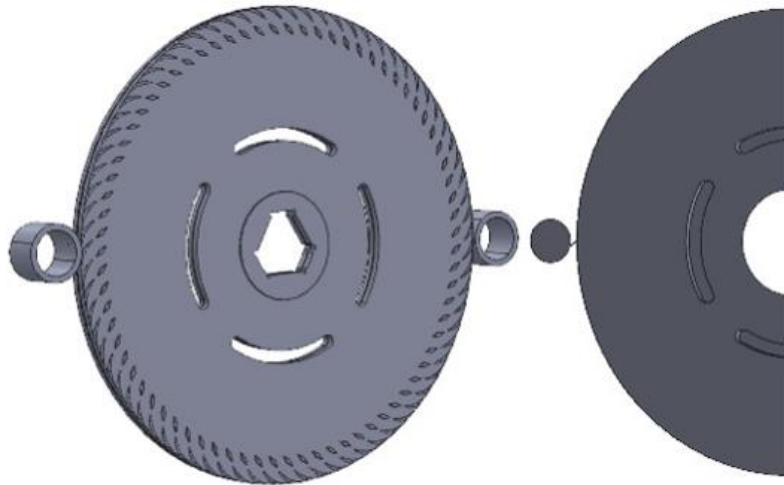


Figure 2.2 Simplified CAD | two disks (left), Half of fluid domain between two disks (right)

2.1.2 Mesh Sensitivity Study

Meshing of the domain is done in a software named Hexpress by Numeca. The domain is divided into 400 cells in the X, 800 cells in the Y and 40 cells in the Z directions, respectively. A mesh sensitivity study is performed to decide the number of cells to be used in each direction. The mesh is refined (Figure 2) at the slot between the upstream nozzle and disk as it is the focus of study here and properties in this region can be captured more accurately. Boundary layer refinement is done on the viscous walls to capture the boundary layers. There are 2.2 million cells in the mesh. A mesh sensitivity study has been conducted to determine the number of cells to be

used. The first level had 200 cells in the X, 300 cells in the Y and 20 cells in the Z directions respectively whereas the next levels had 100 cells more in the X, 200 cells more in the Y and 10 cells more in the Z directions, respectively. The increase in mass flow is found to be insignificant after the fourth as shown in Table 2.1. Therefore, mesh level 3 is used in all cases.

Table 2.1: Mesh Sensitivity Study

Mesh level	Number of cells	Mass flow rate of half disk (kg/s)
1	326,025	0.000109
2	1,497,600	0.00011048
3	2,247,383	0.00011054
4	3,893,679	0.00011056

To ensure the accuracy of the simulation, a mass flow convergence study was conducted to verify mass conservation within the Tesla turbine model. This process involved checking that the mass flow rate at the inlet was nearly equal to the mass flow rate at the outlet as shown in Figure 2.3. Although not exactly equal, the close agreement in mass flows indicates that the CFD model is capturing the steady-state behavior of the flow with sufficient precision. This convergence verification reinforces the reliability of the results for further analysis of the turbine's performance and efficiency.

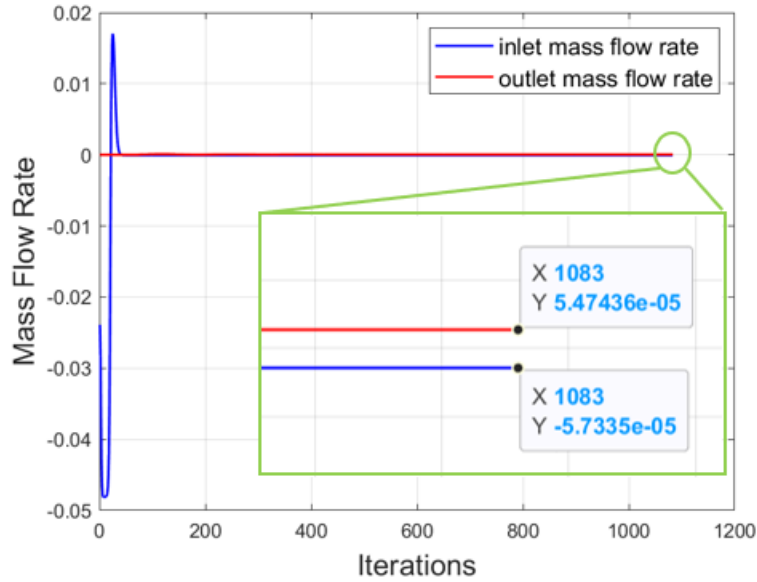


Figure 2.3 Mass Flow Convergence

2.1.3 Numerical Setup

CFD simulations are done in ICFD++ software from Metacomp and simulations are run on the NCSU HPC environment. All the boundary conditions are shown in Figure 2.4. Simulations are run at inlet stagnation pressures of 2bar, 5bar and 8bar with a stagnation temperature of 300 K and a back pressure of 1 bar. Rotor speeds of 0, 5000, 8000, 10,000 and 15,000 RPM were incorporated at each inlet pressure. For post-processing, the software Tecplot is employed. A nozzle-rotor simulation strategy is subsequently implemented to consider the small gap between the disk and the housing, as depicted in Figure 2.5. Here, the upstream nozzle and the nozzle slot are not rotating, and the disk represents the moving rotor. To verify the correctness of this implementation, contours of angular velocity (ω) are examined. In this configuration, the stator is expected to have a rotational speed of 0 rad/s, while the rotor is set to rotate at 524 rad/s. The observed scenario matches these specifications accurately, confirming the correct implementation of the CFD simulation.

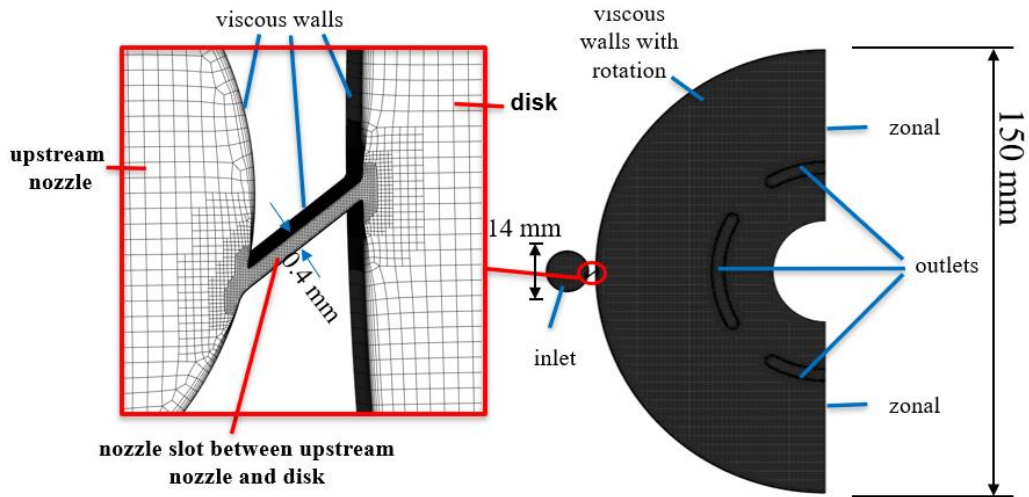


Figure 2.4 Mesh refinement and boundary conditions

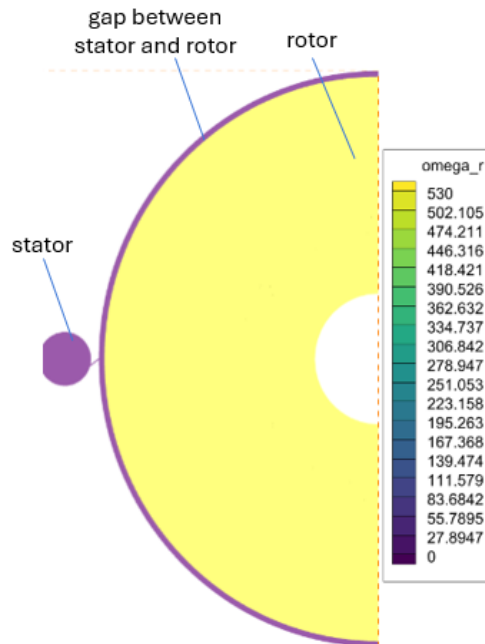


Figure 2.5 Angular velocity contour of the stator-rotor case with a rotational speed of 5000 RPM

Figure 2.6 compares the simulation results of a full-disk domain (right) with a half-disk domain (left). In the half-disk case, the domain has been duplicated, rotated, and adjusted in Tecplot to visually reconstruct a full disk. The primary distinction between the two cases lies in the use of zonal boundary conditions in the half-disk simulation. The flow follows a spiral path in both cases, indicating that the zonal boundary conditions maintain the expected flow behavior. However, discrepancies are observed in the torque and power values between the two simulations.

These differences can likely be attributed to slight variations in the radial and tangential velocity contours between the cases. Both these cases are for an inlet pressure of 2 bar and a rotational speed of 5000 RPM.

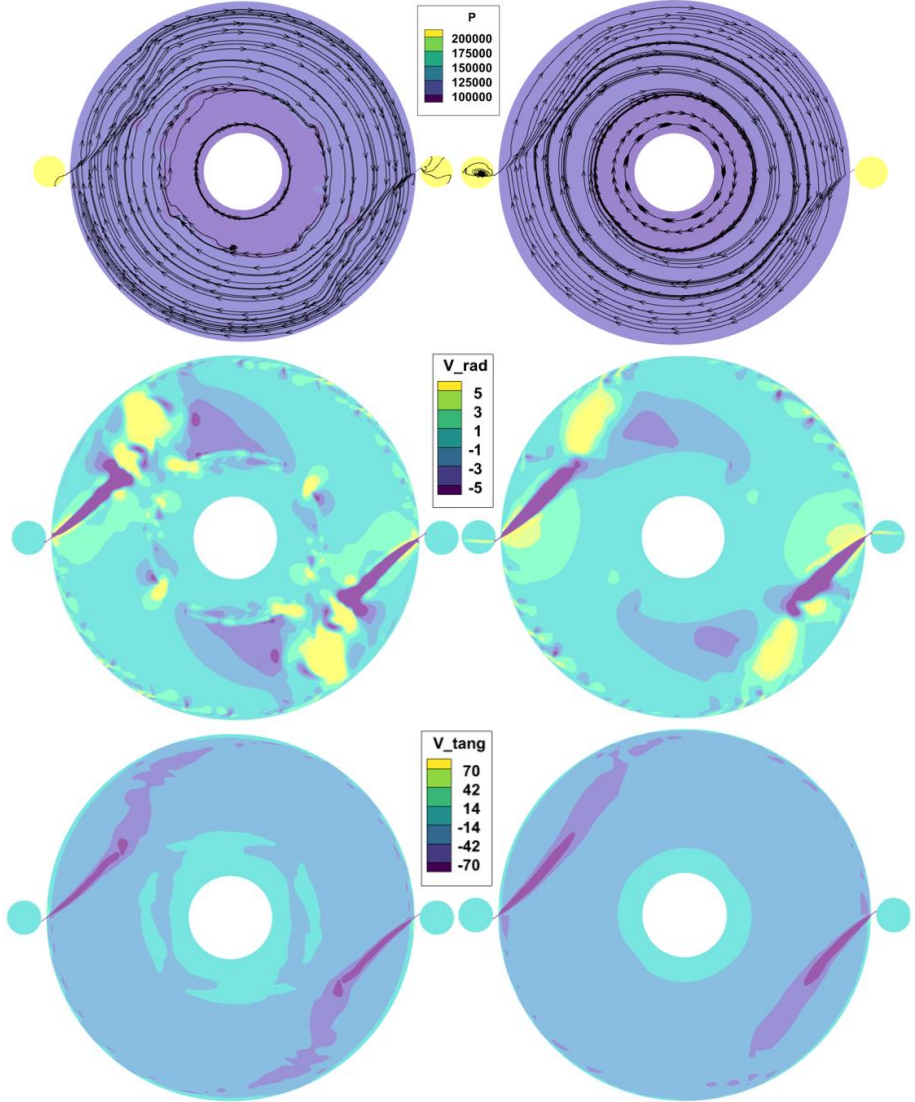


Figure 2.6 Streamlines (top), Contours of Radial Velocity (middle) and Tangential Velocity (bottom) in simulations of half disk (left) vs. full disk (right)

2.2 Baseline CFD Results

2.2.1 Flowpath

Figure 2.7 presents the streamlines along the wall of the disk under two distinct conditions: a) at 0 RPM and b) at 5000 RPM, both corresponding to an inlet stagnation pressure of 2 bar. Notably, a spiral flow path is evident in the case with 5000 RPM, providing compelling evidence for the accuracy of the simulations. This observed spiral flow path is consistent with the expected behavior for a Tesla turbine, where the flow follows a spiral trajectory from the inlet to the outlet before exiting. This alignment between expected and observed flowpath validates the fidelity of the simulation setup, ensuring reliable results for subsequent analysis and interpretation.

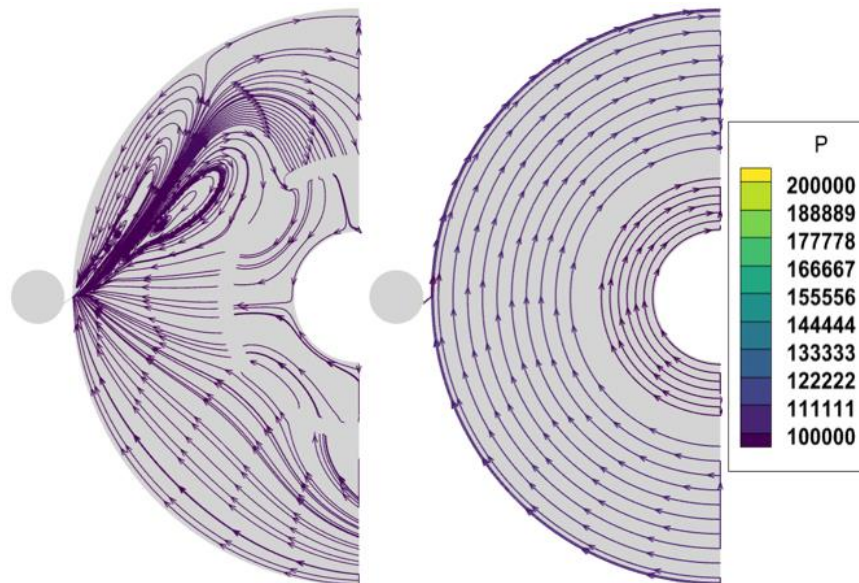


Figure 2.7 Static Pressure streamlines on disks at inlet stagnation pressure of 2 bar and rotational speed of 0 RPM (left) 5000 RPM (right)

Shear lines which are colored according to static pressure on the walls of the disk are plotted in Figure 2.8. The flow travels further with increasing inlet stagnation pressure. This enhanced interaction results in a larger shear stress on the wall and higher torque. This can be additionally attributed to a higher nozzle exit velocity at higher pressure ratios.

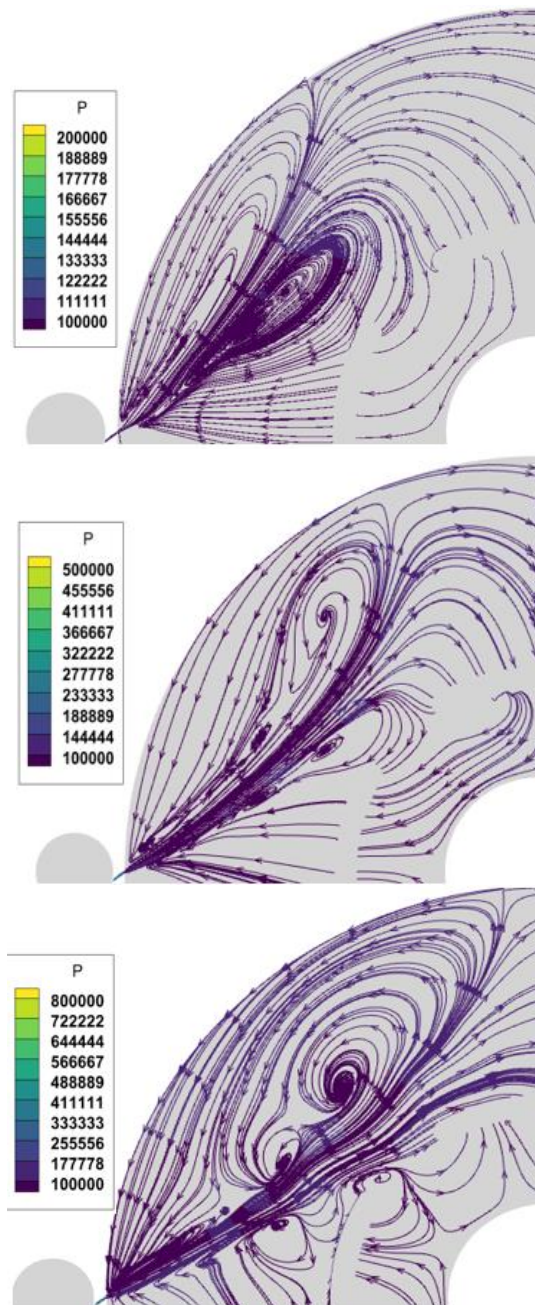


Figure 2.8 Static Pressure streamlines on the disk at zero rotational speed and inlet stagnation pressure of 2 bar (top), 5 bar (middle), 8 bar (bottom)

Indeed, the same trend can be observed in static pressure contours as well. Figure 2.9 below depicts static pressure contours at 5000 rpm for inlet stagnation pressure of 2 bar, 5 bar and 8 bar.

The size of the jet produced at the disk's inlet increases with the increase in stagnation pressure ratio.

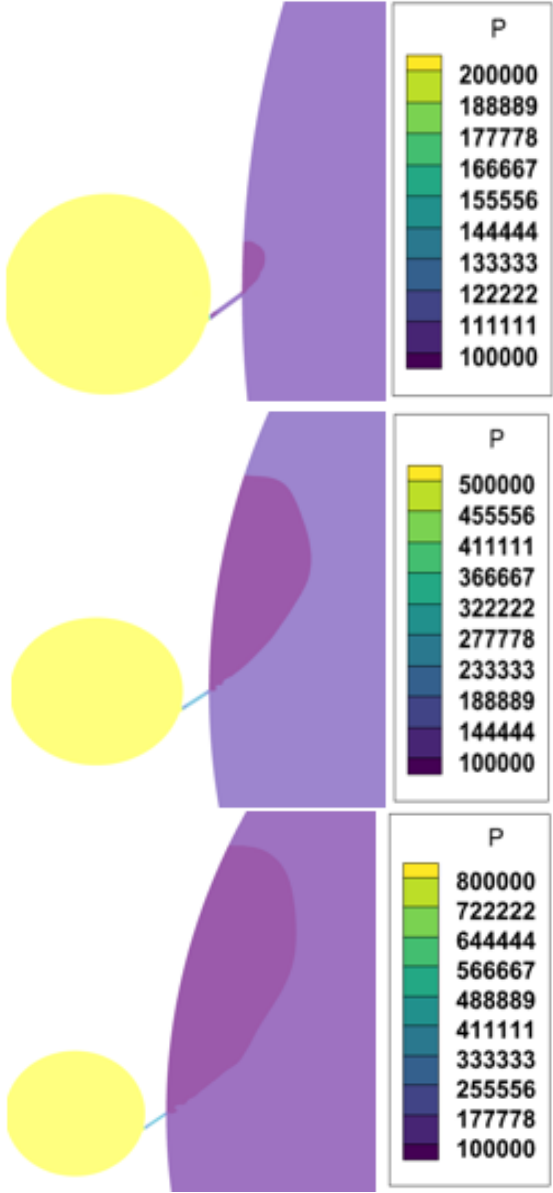
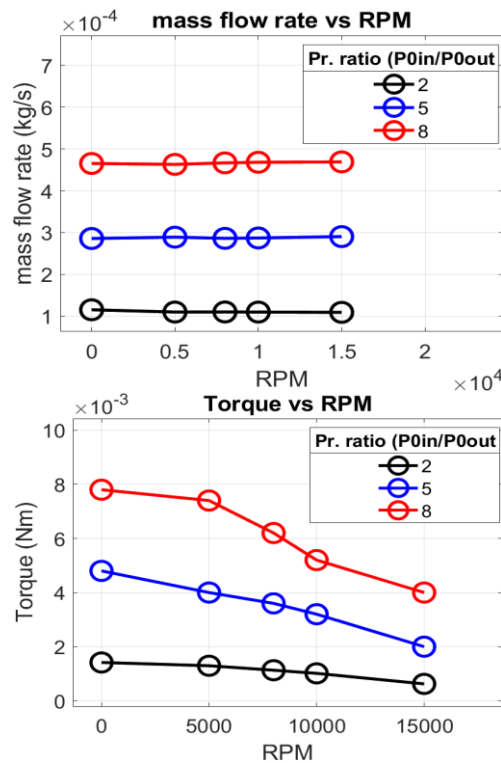


Figure 2.9 Static Pressure on the disk wall at inlet stagnation pressures of 2bar (top), 5bar (middle), 8bar (bottom)

2.2.2 Performance Characteristics

Variations in inlet mass flow rate, torque, and power across different inlet pressures and rotational speeds (RPMs) for a single disk of the turbine for the nozzle-rotor simulation are plotted.

As evident from the equation (12), mass flow increases with higher inlet stagnation pressures and is independent of RPM. Torque follows the same trend as torque is directly proportional to the mass flow rate. Power increases with increase in pressure and RPM and tends towards its maximum for a given mass flow rate which can in Figure 2.10. While the plots in Figure 6 provide valuable insights into the behavior of the turbine under different conditions, they may not be sufficient to pinpoint the optimal operating point. To comprehensively assess turbine performance and determine the most favorable operating conditions, additional turbine characteristics need to be analyzed and plotted which will be discussed later in this section.



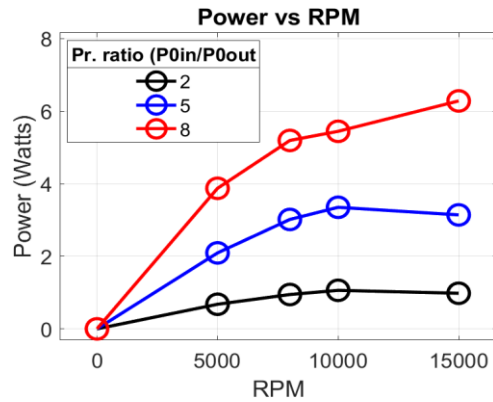


Figure 2.10 RPM (X) vs. (Y) mass flow rate (top), Torque (middle), Power (bottom) at various inlet stagnation pressures and disk RPMs.

2.2.3 Reynolds Number

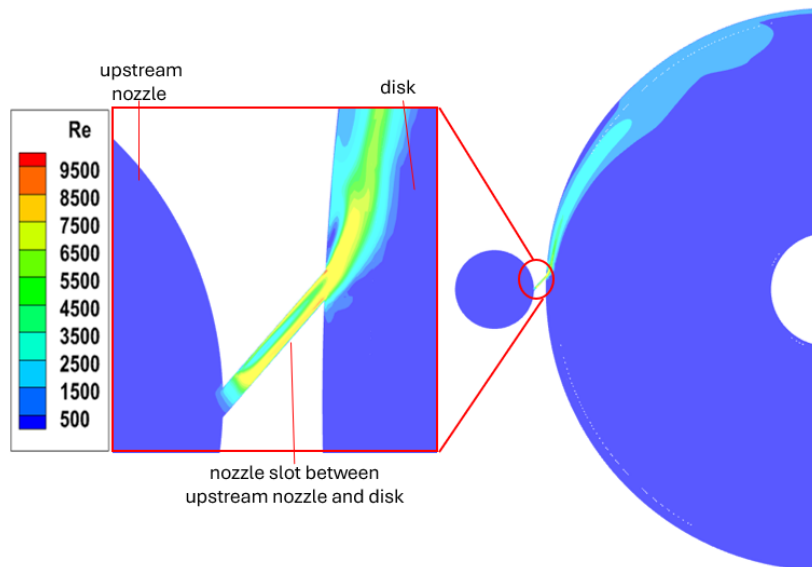


Figure 2.11 Reynolds Number contour at the midpoint between two disks at an inlet pressure of 2 bar and 0 RPM.

Figure 2.11 shows a Reynolds number contour plot at the midpoint between two disks, obtained at a two-bar inlet pressure and 0 rpm. The main plot highlights the flow region between the upstream nozzle and the disk, with a close-up showing the nozzle slot. High Reynolds numbers are observed near the nozzle slot, exceeding 4000, which indicates turbulent flow as the fluid exits the nozzle. As the fluid moves into the gap between the two disks, the Reynolds number decreases, transitioning from turbulent to more laminar flow. This pattern aligns with expected flow behavior, as turbulence gradually subsides, and the laminar flow develops within the inter-disk region.

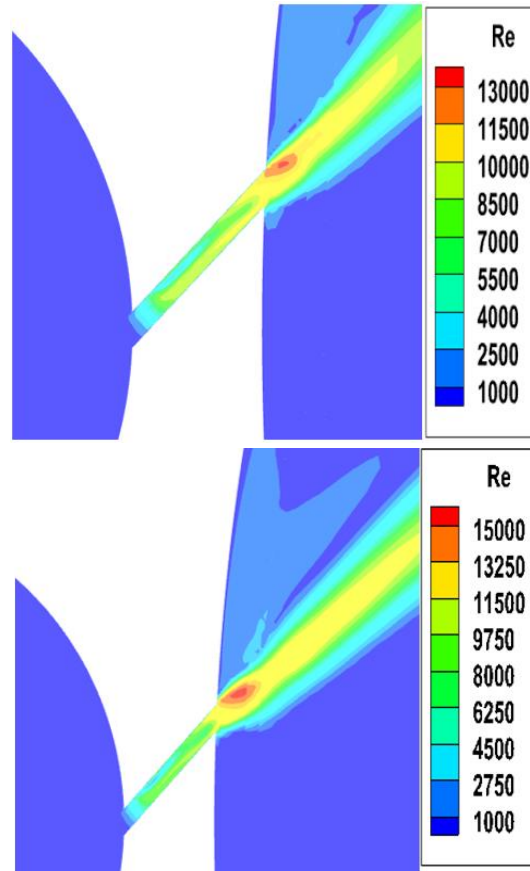


Figure 2.12 Reynolds Number contour at the midpoint between two disks at 0 RPM and inlet pressure of 5 bar (top) and 8 bar (bottom)

Figure 2.12 displays Reynolds number contour plots at the midpoint between two disks for inlet pressures of 5 bar (top) and 8 bar (bottom), both at 0 rpm. As seen, the Reynolds number increases with higher inlet pressures, leading to more pronounced turbulent regions near the nozzle slot. At 5 bars, the flow shows elevated Reynolds numbers near the nozzle exit, indicating turbulent flow that gradually transitions to laminar as it moves into the inter-disk space. The effect is even more pronounced at 8 bars, where the Reynolds number further increases, intensifying turbulence at the inlet region before it stabilizes in the disk gap. This trend confirms that an increase in inlet pressure/pressure ratio amplifies turbulence.

2.2.4 Laminar vs. Turbulent

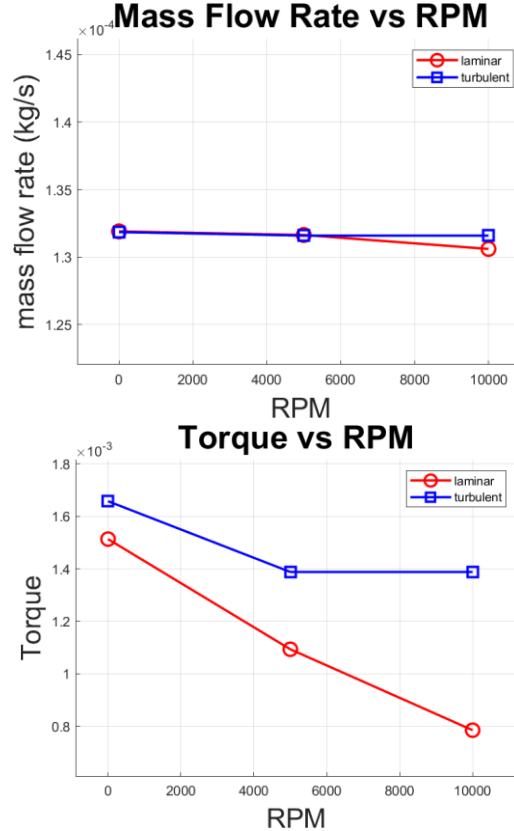


Figure 2.13 RPM (X) vs (Y) mass flow (top) and torque (bottom) for laminar and turbulent flows

The plots of mass flow and torque against rpm for both laminar and turbulent flow conditions in the Tesla turbine can be seen in the above Figure 2.13 which reveal that mass flow remains nearly constant as rpm increases, indicating that rpm has minimal influence on the rate of fluid passing through the turbine. In contrast, torque decreases with increasing rpm for both flow conditions, with the decline being more pronounced in the laminar flow. The use of a turbulence model in CFD simulations results in an increase in torque, as turbulence promotes greater energy transfer between fluid layers, leading to higher frictional forces and enhanced interaction with the turbine blades.

2.2.5 Relative Flow Angle

Next, the flow angles are investigated. Figure 2.14 shows the velocity triangle at the rotor inlet for and Figure 11b depicts the flow angle the power, and reveals optimal relative flow angles between 7 and 17 degrees and is dependent on the pressure ratio. For a pressure ratio of 5, which corresponds to an isentropic Mach number of 1.71, optimal flow angle was 18 degrees.

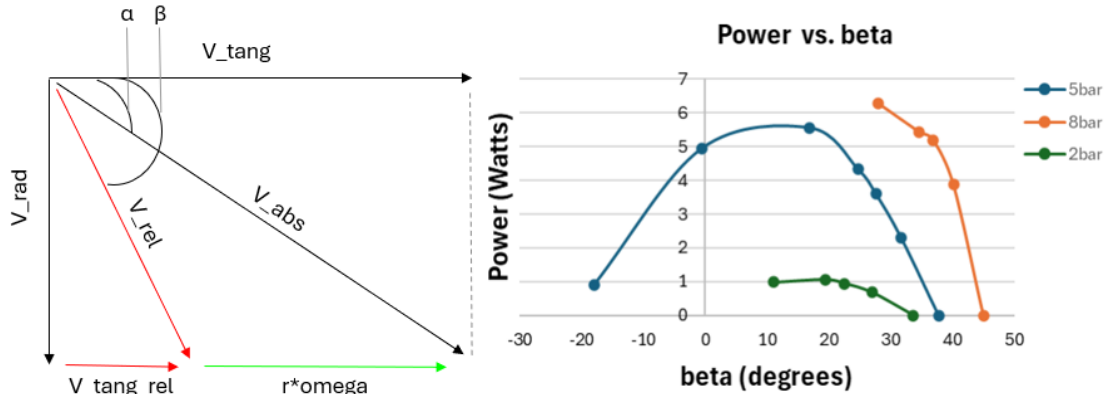


Figure 2.14 Velocity triangle at rotor inlet (left), Power vs. Reactive flow angle at different inlet stagnation pressures (right)

2.2.6 Boundary layer

Finally, since shear stress is the primary driver of power, the boundary layer is investigated. The boundary layer development in the left side of the nozzle slot can be seen in the Figure 2.15 with the axial velocity profile of the fluid towards the nozzle center and the boundary layer for the case of 5bar at a rotational speed of 5000 RPM. The boundary layer thickness is approximately 0.05 mm, determined from the velocity profile as the distance where the velocity reaches a constant value.

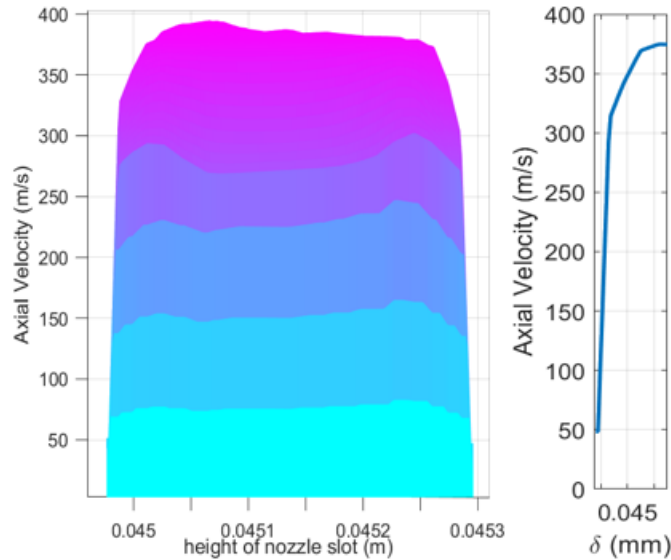


Figure 2.15 Axial Velocity profile of fluid in the nozzle (left) Boundary layer on left side of the nozzle (right)

2.2.7 Turbine Characteristics

The Turbine characteristics for the nozzle-disk simulations are depicted in Figure 2.16. Left shows the relationship between total pressure ratio at inlet to outlet plotted against mass flow parameter which is the product of mass flow rate and inlet stagnation temperature divided by inlet stagnation pressure. The plot shows that the inlet is choked as the mass flow parameter is independent of the pressure ratio at higher pressure ratios. From Figure 2.10, it is clear that higher power output is achieved at higher inlet pressures. However, right Figure 2.16 (right) shows a relatively little dependence of inlet pressure on specific power. They are used for scaling at relevant pressures / working fluids as well, the mass flow rate at a particular inlet pressure can be calculated and the corresponding power output can be derived from the mass flow parameter versus specific power plot at a specific pressure ratio. For example, for a case of 60 bar in and 30 bar out pressure power extraction would be 448 watts at a mass flow of 0.0896 kg/s.

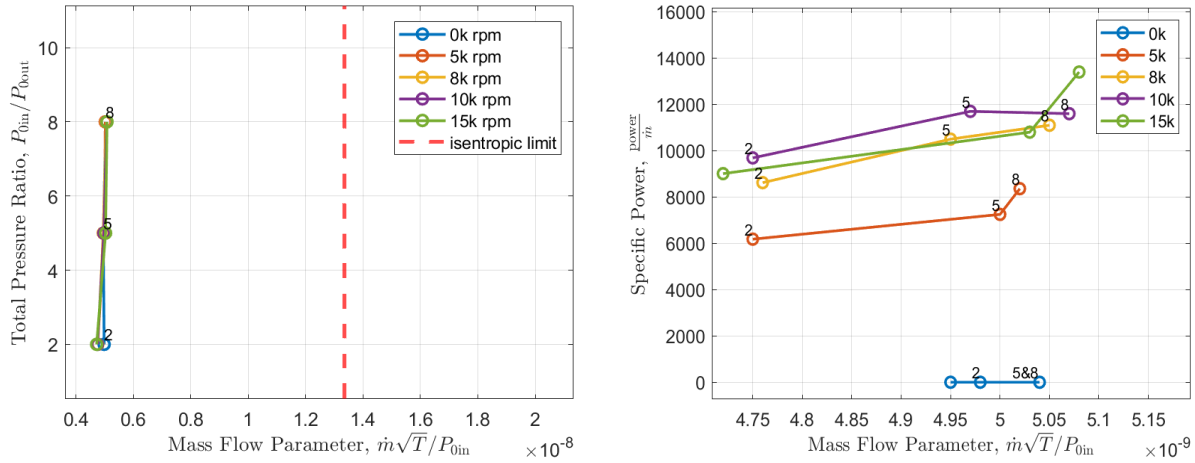


Figure 2.16 mass flow parameter (X) vs. total pressure ratio(left), specific power at various inlet stagnation pressures and disk RPMs (right)

This chapter presented the fluid domain and CFD modeling of the Tesla turbine, including an analysis of mesh sensitivity. Various numerical results were discussed, highlighting how performance characteristics of the turbine vary under different operating conditions and flow parameters. The turbine's performance characteristics were plotted based on the CFD results. These findings form the foundation for the subsequent chapter on nozzle optimization.

CHAPTER 3

Nozzle Optimization

Chapter 2 focuses on nozzle optimization and investigates how variations in the contour of the nozzle slot, the inclination of the nozzle slot, and the number of nozzles influence the performance of the Tesla turbine. By exploring these parameters, the chapter aims to optimize the turbine's design for improved efficiency and power output under different operating conditions.

3.1 Nozzle Contour Variation

Figure 3.1 Mach contour of the fluid on slot between upstream nozzle and disk at inlet stagnation pressures of 2bar shows the contours of Mach number in the fluid in the slot between upstream nozzle and disk and we can observe flow choking in all cases. Mass flow rate is maximum when the flow is choked i.e., at $M=1$ and is described in equation (13). A in equation (12) is the area of the throat of the nozzle slot between upstream nozzle and disk (rotor). The throat here is a rectangle of dimensions 0.4mm x 0.5mm, where 0.5 mm is the gap between the disks and 0.4 mm is the height of the slot.

$$\dot{m} = \frac{AP_t}{\sqrt{T_t}} \sqrt{\frac{\gamma}{R}} \left(\frac{\gamma + 1}{2} \right)^{\frac{-\gamma+1}{2(\gamma+1)}} \quad (13)$$

Table 3.1: Coefficient of Discharge

Inlet Stagnation Pressure (bar)	Choked Mass Flow Rate (kg/s) (Ideal)	Mass Flow Rate from CFD (kg/s) (Actual)	Coefficient of Discharge (Cd)
2	18.66E-05	10.76E-05	0.58
5	4.66E-04	2.80E-04	0.60
8	7.46E-04	4.48E-04	0.60

Table 3.1 presents the choked mass flow rates achievable for a single disk at inlet stagnation pressures of 2 bar, 5 bar, and 8 bar, alongside the corresponding mass flow rates obtained from CFD simulations for a rotational speed of 0 rpm for the flat nozzle slot configuration. Additionally, the compressible coefficient of discharge (C_d) which is the ratio of mass flow rate from CFD to choked mass flow rate is provided for each case.

$$\text{Coefficient of Discharge } (C_d) = \frac{\text{actual mass flow rate}}{\text{ideal mass flow rate}} \quad (14)$$

Table 3.1 clearly shows that the mass flow rates obtained from CFD simulations are lower than the choked mass flow rates for the flat nozzle configuration. This observation suggests that there may be room for improvement in the nozzle design. To explore this further, the nozzle configuration is altered from flat to CD (converging-diverging) to assess its potential impact on the coefficient of discharge (C_d).

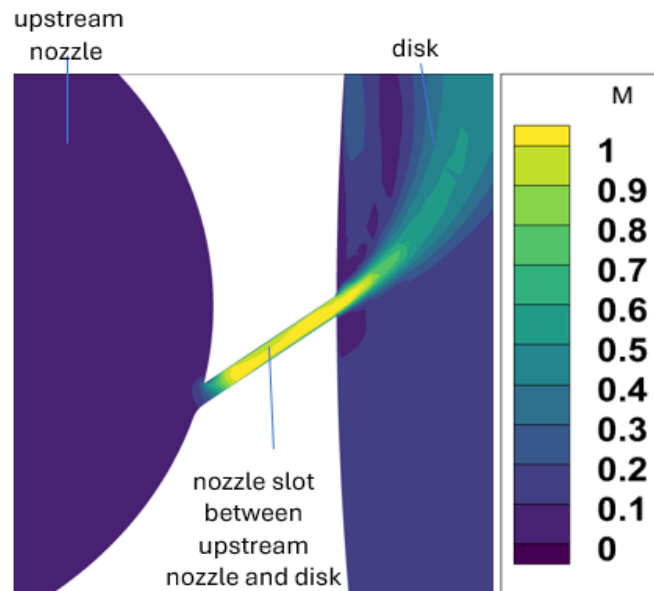


Figure 3.1 Mach contour of the fluid on slot between upstream nozzle and disk at inlet stagnation pressures of 2bar

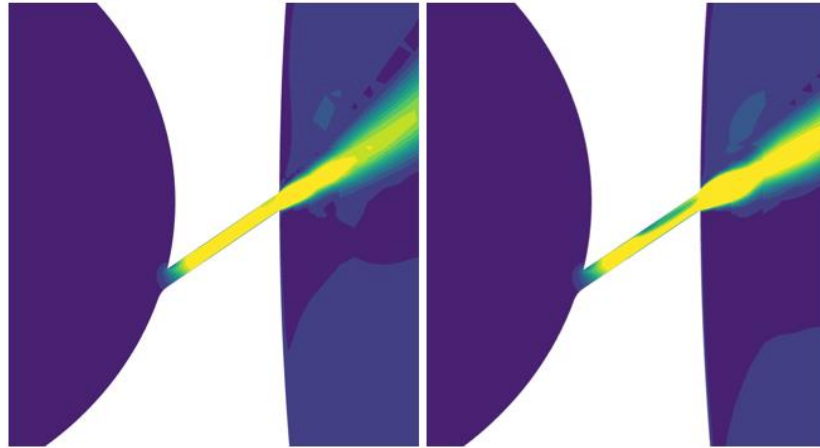


Figure 3.2 Mach contour of the fluid on slot between upstream nozzle and disk at inlet stagnation pressures of 5bar (left), 8bar (right)

In Figure 3.4, four designated stations serve as focal points for investigating total pressure and total pressure loss. Station 1 represents a point within the domain, situated before the slot and at the upstream nozzle's exit. Moving along, Station 2 marks the entry of the slot, while Station 3 denotes its exit, and Station 4 stands at the disk's entrance. The configuration of the slot has been altered, transitioning from a flat design to a convergent-divergent profile. This adjustment aims to assess whether such a modification can mitigate the loss in total pressure.

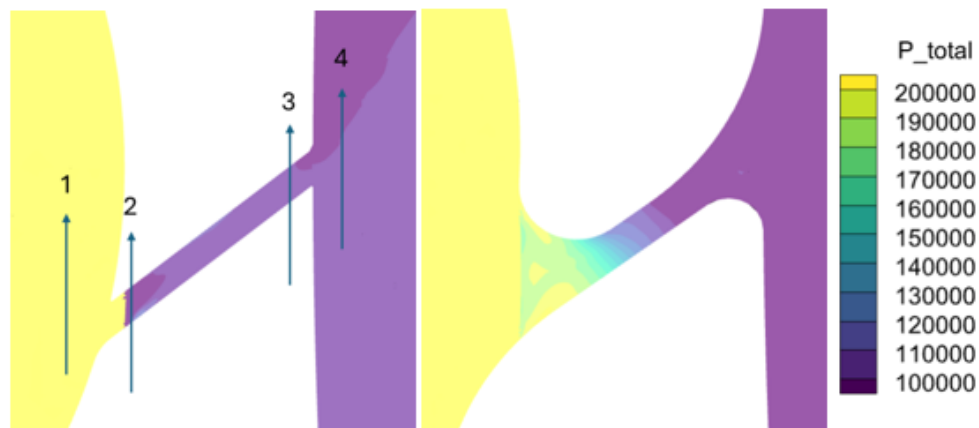


Figure 3.3 Total Pressure contour on the slot between upstream nozzle and disk for flat (left) and CD (convergent divergent) (right) configurations with an inlet stagnation pressure of 2 bar

In the flat case, the total pressure declined from 2 bar to approximately 1.6 bar, while in the convergent-divergent configuration, it decreased to approximately 1.75 bar, as depicted in Figure 3.5, across the span from station 1 to station 4. Notably, the ratio of pressure loss to inlet pressure exhibited a reduction from 0.21 (in the flat case) to 0.14 (in the convergent-divergent case), as illustrated in Figure 3.4. The coefficient of discharge, indicative of the ratio between the actual mass flow rate (derived from CFD simulations) and the ideal mass flow rate, demonstrated a notable increase of approximately 0.15 across all cases. This observation is clearly depicted in Figure 9a.

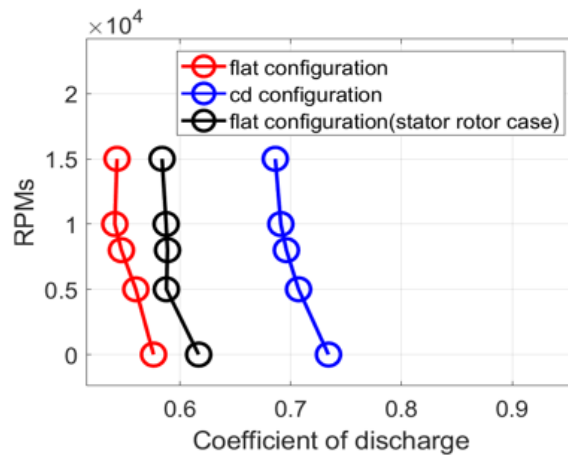


Figure 3.4 Coefficient of discharge (X) vs. RPM (Y)

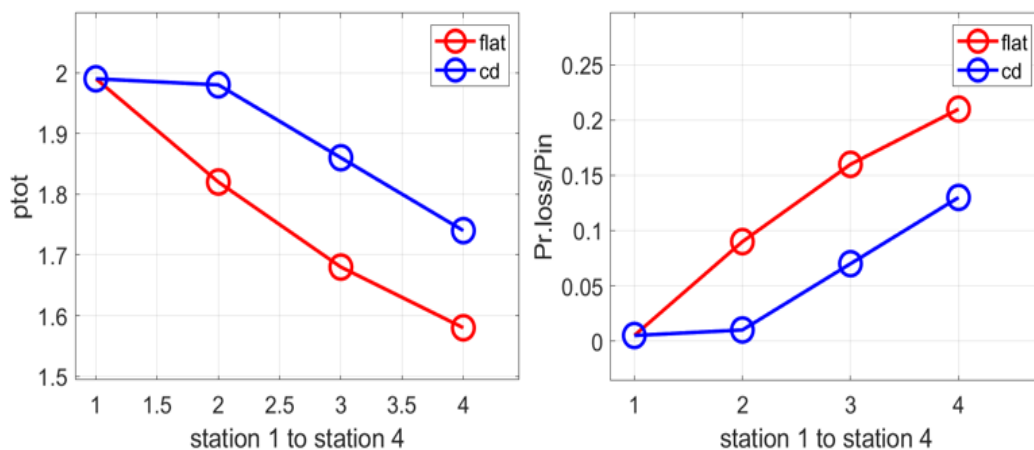


Figure 3.5 Total pressure (left), Ratio of total pressure loss to inlet total pressure (right) from Station 1 to Station 4

3.2 Nozzle Inclination Variation

The next phase of the study focused on figuring out the optimal inclination angle for the nozzle slot positioned between the upstream nozzle and the disk. This investigation aimed to evaluate the impact of nozzle angles on performance metrics such as mass flow, torque, and power. The inclination angle was varied systematically from 15 to 75 degrees in increments of 5 degrees. The angle being discussed here is illustrated in Figure 3.6. It represents the inclination of the nozzle slot relative to the horizontal axis, which passes through the center of the disk. This angle defines the orientation of the nozzle slot with respect to the horizontal plane, and its variation influences the flow characteristics as the fluid exits the nozzle and interacts with the disk. By adjusting this angle, the study investigates how different flow trajectories impact the performance of the turbine. The setup shown in Figure 3.6 provides a clear visualization of the geometric configuration used in this analysis.

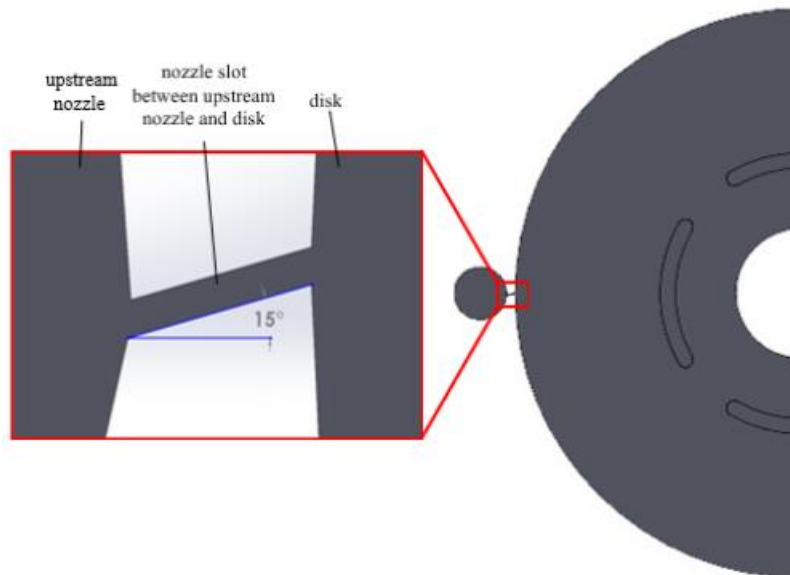


Figure 3.6 Geometry of the nozzle slot with a 15° inclination between the upstream nozzle and disk

For nozzle inclination angles ranging from 15 to 45 degrees, the nozzle slot between the upstream nozzle and the disk was well-accommodated, with the centers of both components aligned along the same axis. However, for angles greater than 45 degrees, adjustments were necessary to

maintain proper alignment. In these cases, the upstream nozzle was moved downward to compensate for the increased inclination. The configurations for the 45-degree and 50-degree cases are shown in Figure 3.7, for the 50-degree nozzle inclination which is the bottom one of Figure 3.7, the upstream nozzle was shifted downward by 1mm.

The meshing of the nozzle and disk geometry was carried out using the macro functions in Hexpress. The meshing process for the initial angle case was performed manually and saved as a macro. This macro was then used to automate the meshing procedure for the subsequent angles, allowing for efficient and consistent meshing across all configurations. By utilizing the macro script, the meshing process was streamlined, ensuring that the grid generation for each nozzle inclination angle from 15 to 75 degrees was executed accurately and with minimal manual intervention.

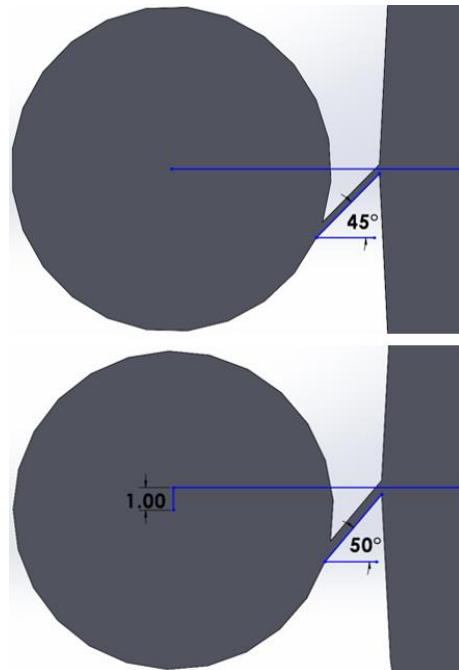


Figure 3.7 Comparison of geometries at inclination of 45 (top) and 50 degrees (bottom)

Figure 3.8 presents the mass as a function of nozzle inclination angles at rotational speeds of 0, 5000, and 10000 RPM. At 0 RPM, the mass flow rate was observed to decrease with an increasing angle up to 45 degrees, followed by a sudden increase at 50 degrees. A similar trend was noted at

both 5000 RPM and 10000 RPM, the mass flow rate initially decreased until 30 degrees, then exhibited a sharp increase at 35 degrees. Afterward, the mass flow rate gradually increased to 50 degrees before decreasing again. The maximum mass flow rate was observed at an inclination angle of 50 degrees.

Similar trends were observed in both torque and power, as shown in Figure 3.9 (top and bottom, respectively). For all three rotational speeds, torque and power initially increased with the inclination angle up to 45 degrees, after which they began to decrease. This resulted in a peak at 45 degrees for both torque and power.

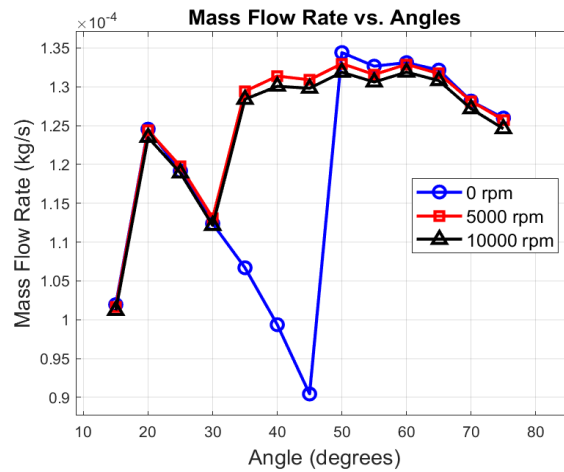
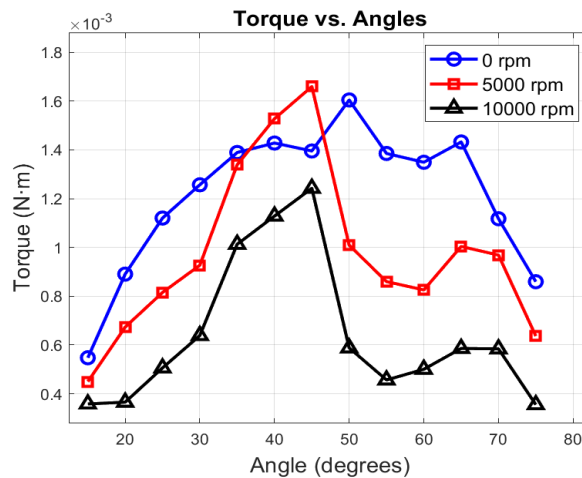


Figure 3.8 Mass flow rate (Y) vs. RPM (X) at different nozzle inclinations



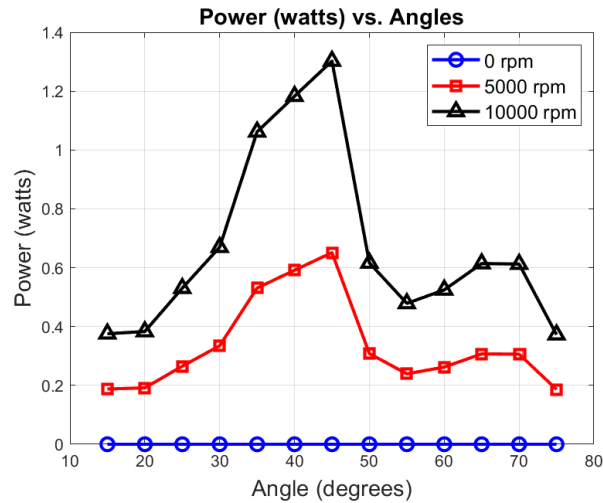


Figure 3.9 RPM (X) vs. (Y) Torque (top), Power (bottom) at different nozzle inclinations



Figure 3.10 Mach contour of the fluid for the 35-degree inclination at 0 RPM (left) and 5000 RPM (right)

Typically, in turbines, the mass flow rate remains constant with increasing RPM. However, as shown in Figure 3.8, for nozzle inclinations of 35, 40, and 45 degrees, the mass flow rate increases with RPM. Figure 3.10 also illustrates the Mach contour of the fluid for the 35-degree inclination at 0 RPM (left) and 5000 RPM (right). At 0 RPM, a significant velocity deficit is observed in the nozzle slot region, forming a large low-velocity pocket due to the turbine’s geometry. This low-velocity region is not present in the 5000 RPM contour, which explains the reduced mass flow rate at 0 RPM. This velocity deficit also explains why torque increased from 0 to 5000 RPM for nozzle

inclination angles of 35, 40, and 45 degrees, contrary to the typical trend of decreasing torque with increasing RPM.

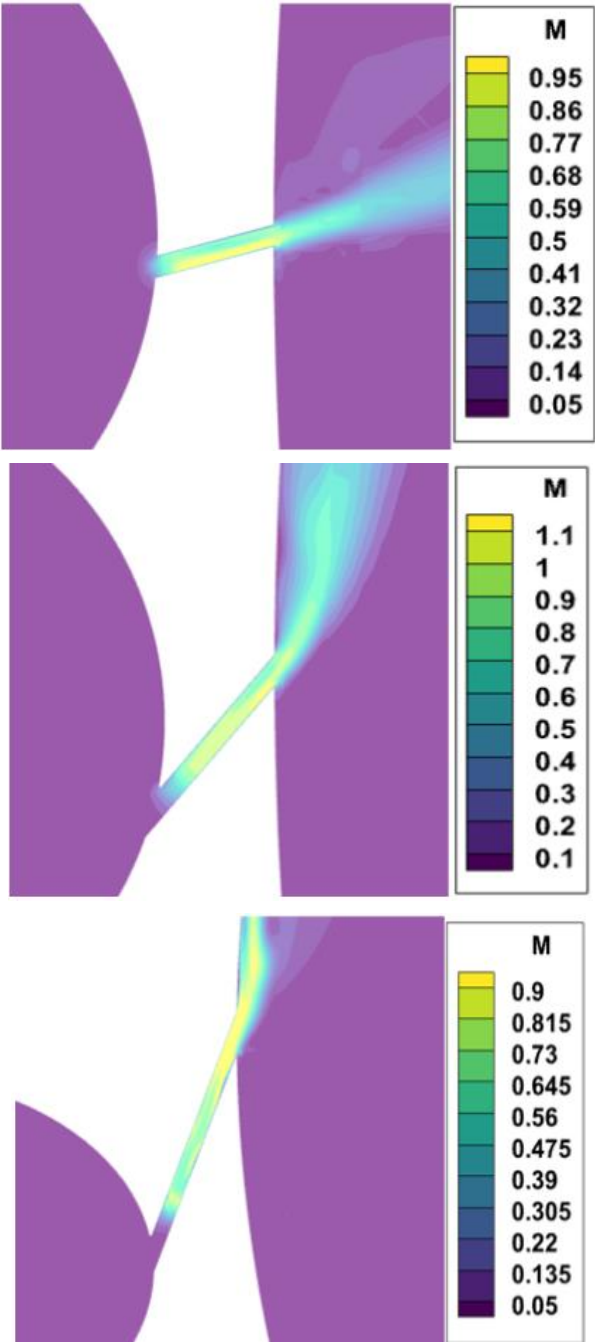


Figure 3.11 Mach contours of the fluid at the nozzle slot for inclination angles of 15 (top), 50 (middle), and 75 (bottom) degrees

Figure 3.11 displays the Mach contours of the fluid at the nozzle slot for inclination angles of 15, 50, and 75 degrees (top, middle, and bottom, respectively). The contours show that full choking

does not occur at 15 and 75 degrees, whereas at 50 degrees, the flow is fully choked. This explains why performance parameters like mass flow, torque, and power are lower at 15 and 75 degrees compared to the optimized 50-degree case.

Figure 3.12 illustrates the variation in torque (left y-axis) and power (right y-axis) with nozzle inclinations, given a mass flow inlet of $7E-5$ kg/s per nozzle. Both metrics show a consistent trend, with values rising to 50 degrees and then declining beyond this point. This pattern indicates at 45 - 50 degrees, the flow conditions reach an optimal alignment, yielding maximum torque and power output before efficiency drops at higher angles, likely due to increasing flow misalignment or energy losses at these inclinations.

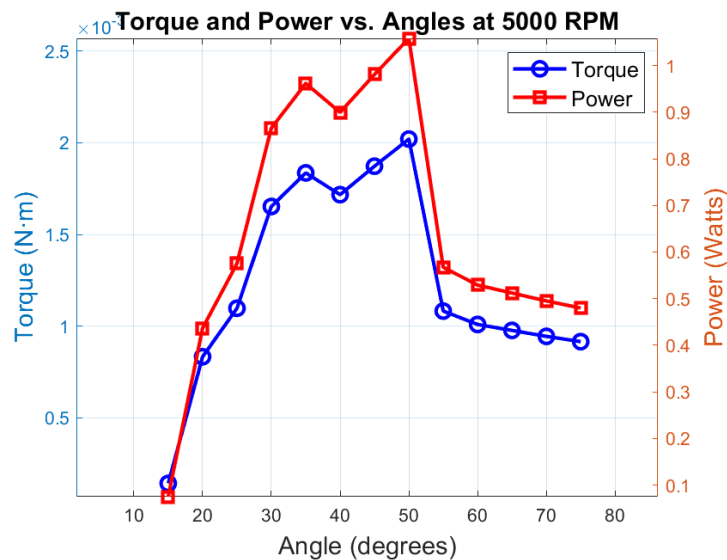


Figure 3.12 Torque (left y-axis) and Power (right y-axis) vs. Nozzle inclinations (X), given a mass flow inlet of $7E-5$ kg/s per nozzle

3.3 Multi Nozzle

Another approach taken to optimize turbine performance involved varying the number of nozzles. Simulations were conducted using four configurations with 2, 4, 6, and 8 nozzles, each positioned equidistantly along the circumference of the rotor. This arrangement ensured consistent spacing between nozzles to promote uniform flow distribution. Figure 3.13 illustrates the fluid domain

between two disks for the configuration with 2 and 4 nozzles (left and right respectively), providing a clear view of the flow channels and nozzle alignment.

To streamline the meshing process, the fluid domain was divided into distinct components based on their geometry. Macros were developed to automate the meshing of components with similar geometries, such as the nozzle, ensuring consistency and efficiency across different simulations. By reusing the same mesh for the inner disk in all cases, the process was further simplified and optimized. The individual meshes for each component were then combined within the CFD++ software to set up the complete CFD model. This approach significantly reduced the time required for meshing while maintaining the accuracy and integrity of the simulation.

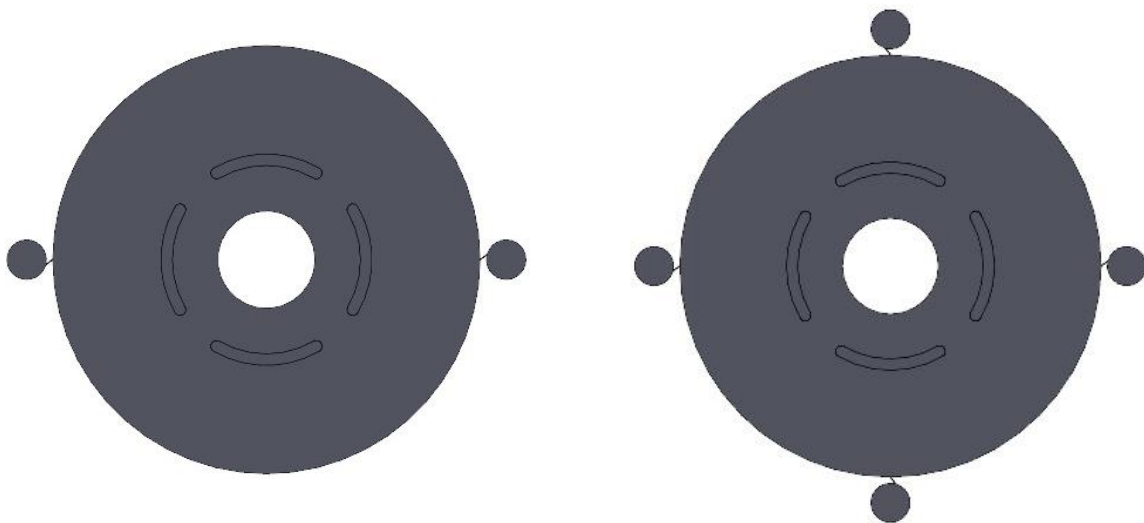


Figure 3.13 Fluid domain between two disks for the configuration with 2 (left) and 4 (right) nozzles

As expected, mass flow, torque, and power all increase with the increase in the number of nozzles. Figure 3.14 presents the mass flow rate plotted against power, illustrating two distinct cases. The blue line represents cases where the pressure ratio was increased from 2 to 5 and then to 8, with a constant configuration of 2 nozzles. In contrast, the red line shows cases where the inlet pressure was held at 2 bar while the number of nozzles was increased sequentially from 2 to 4, 6, and finally 8. The results indicate that increasing the pressure ratio has a more pronounced effect on power output compared to increasing the number of nozzles.

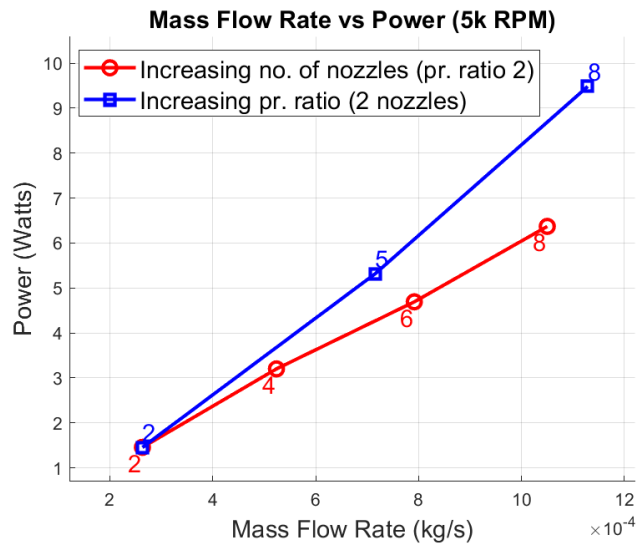


Figure 3.14 Mass flow rate (X) vs. Power (Y)

CHAPTER 4

Experiment

This chapter focuses on the experimental setup and the validation process used to verify the accuracy of the CFD model developed for the Tesla turbine. The experiment's goal is to compare the turbine's performance under controlled conditions with the predictions made by the numerical simulations. By running a series of tests on a physical prototype, we can assess the model's reliability and identify any discrepancies between the simulated and real-world behavior. This experimental validation is critical for ensuring that the CFD model provides an accurate representation of the turbine's performance, and it lays the foundation for further optimization in the design process.

4.1 Experimental set-up

The experiments were conducted in two stages to evaluate the prototype's performance under different operating conditions. In the first stage, the prototype was tested using a 100-watt generator, provided by the sponsors along with it. This setup allowed for initial validation and testing at lower power levels. In the second stage, the experiment was repeated using an 800-watt generator.

Experimental set-up with the small generator can be seen in the Figure 4.1. It consists of a compressed air inlet, which supplies air to drive the turbine. A pressure meter is installed to monitor the inlet pressure, ensuring consistent operating conditions. The turbine is coupled to a generator, which converts mechanical energy into electrical energy. A tachometer is used to measure the rotational speed (RPM) of the turbine, while a multimeter is connected to measure the voltage across from the generator. Load resistors are connected in parallel to simulate different electrical loads.

4.1.1 Smaller Generator Test

The first set of experiments was conducted with three different load settings: one resistor, two resistors, and six resistors. Air was introduced into the system at each load configuration until the pressure meter indicated a constant value. These tests were performed at three distinct pressure levels: 1 bar, 1.5 bar, and 2 bar. Additionally, tests were conducted at 1 and 1.5 bar under no-load conditions too. During each experiment, voltage and speed were recorded for all runs. The results of these experiments are presented in Table 4.1 below. The current was then calculated using Ohm's law, considering the individual resistors' resistance and the equivalent resistance of the parallel resistor configuration. This approach allowed for precise determination of the electrical current drawn during each test, enabling a thorough analysis of the prototype's performance under varying load and pressure conditions.

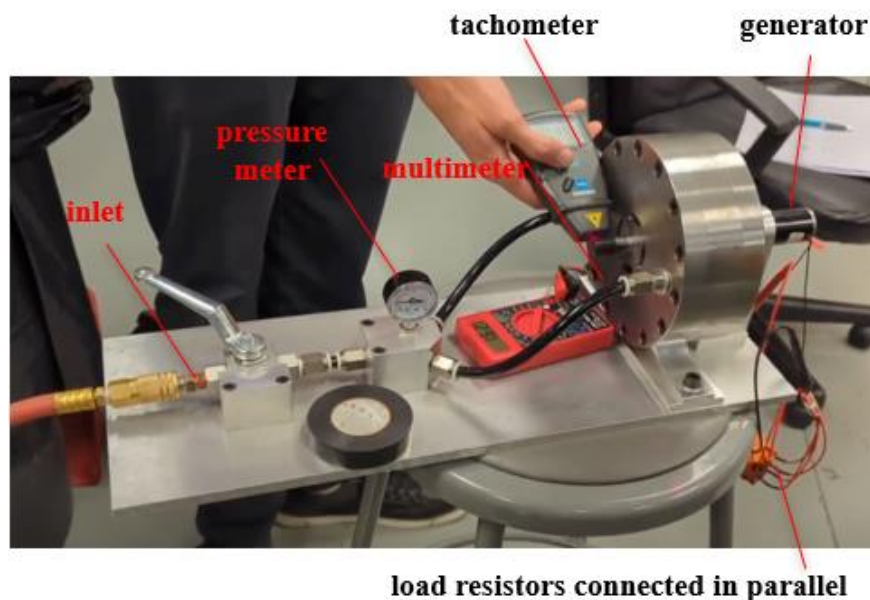


Figure 4.1 Experimental setup 1 of Mark-1

Plot in Figure 4.2 shows relationship between power and rpm for first experiment. As the number of resistors increases, the power output decreases for a given RPM, with higher RPMs producing more power across all cases.

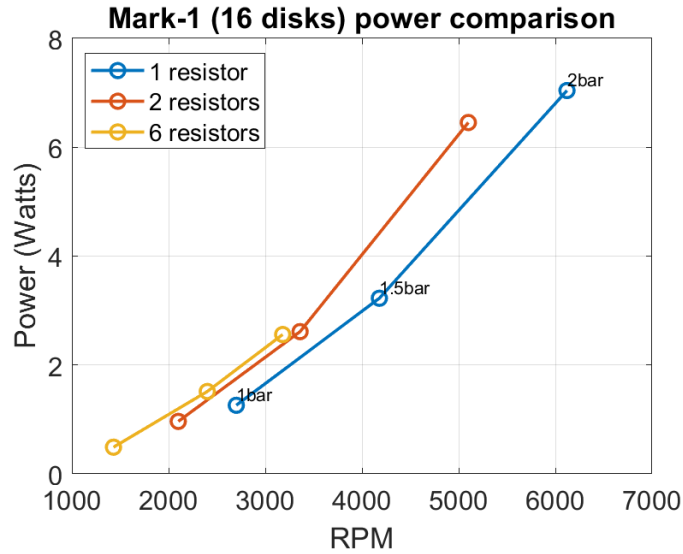


Figure 4.2 Power (Y) vs RPM (X) for Experiment -1

Table 4.1: Experiment-1 Results

No. of resistors connected	Pressure (bar)	Speed (RPM)	Voltmeter reading V (volts)	Resistance R (ohms)	Current I = V/R (Amps)	Power P = VI (Watts)
0 (No load)	1	3920	5.63	NA (Not Applicable)	NA	NA
	1.5	8600	12.30			
1	1	2700	2.75	6	0.46	1.26
	1.5	4180	4.40		0.73	3.23
	2	6120	6.50		1.08	7.04
2	1	2100	1.70	3	0.57	0.96
	1.5	3360	2.80		0.93	2.61
	2	5100	4.40		1.47	6.45
6	1	1430	0.70	1	0.70	0.49
	1.5	2400	1.23		1.23	1.51
	2	3180	1.60		1.60	2.56

4.1.2 Bigger Generator Test

Experimental setup of the second set of experiments with 800-watt generator used to measure power and the other change being an additional multimeter connected in series at one terminal of the generator to measure the current is shown in Figure 4.3 *Experimental setup 2 of Mark-1*. A motor mount and coupling were 3D printed to accommodate the bigger size of the 800-watt generator.

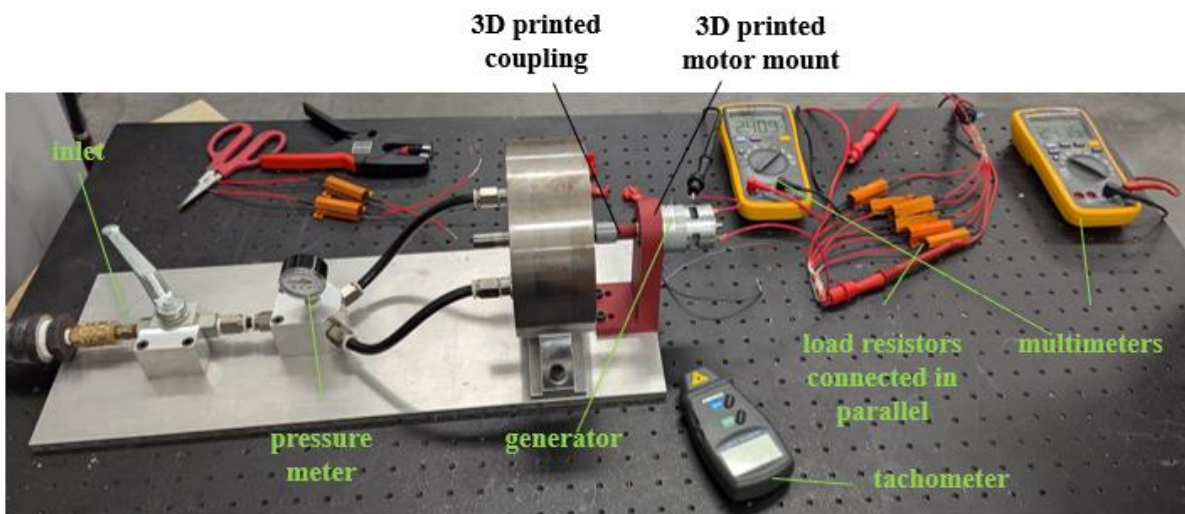


Figure 4.3 Experimental setup 2 of Mark-1

The second set of experiments were conducted with no load, 1, 2, 4, 6 and 8 resistors, all the resistors connected in parallel to the generator. Various pressures were tested at each load condition and the different run values are tabulated in Table 4.2.

Figure 4.4 shows the plots of current and voltage versus pressure for various load conditions. The top plot illustrates current against pressure, while the bottom plot depicts voltage against pressure. The data reveals that, as expected, the generator draws more current at a given pressure when the load increases, whereas the voltage drops with higher loads. This behavior aligns with Ohm's Law ($V = IR$) and indicates that, under greater loads (lower resistance), the generator compensates by delivering more current, though the voltage output reduces.

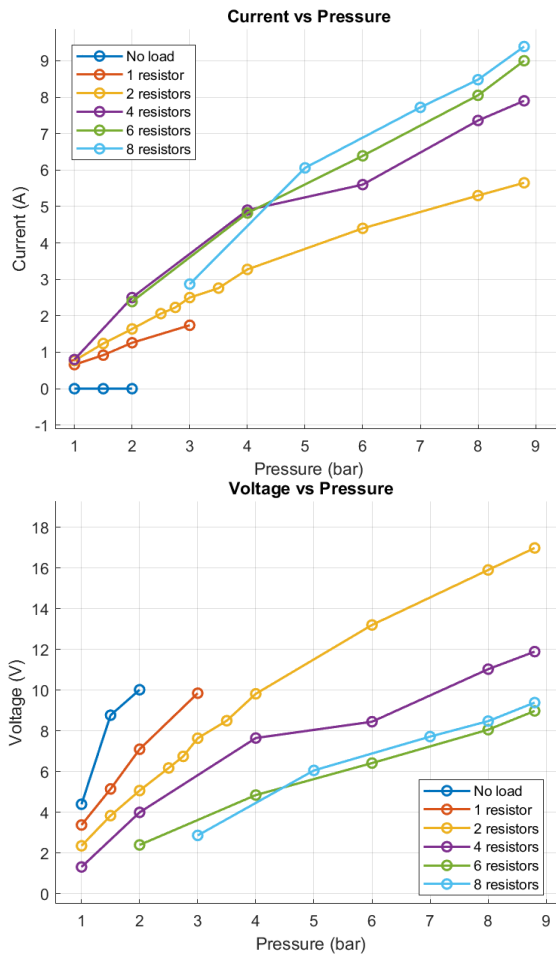


Figure 4.4 Pressure (X) vs. (Y) Current (top) and Voltage (bottom) for Experiment-2

The graph in Figure 4.5 illustrates the relationship between current and speed for various resistor configurations. As the number of resistors increases, the current drawn by the motor decreases for a given speed, demonstrating the impact of resistive load on motor performance.

These observations suggest that the generator's power output is behaving as expected, with current increasing and voltage decreasing as load increases. This alignment with anticipated trends indicates that the experiment is progressing in the correct direction, as the generator's response to varying loads matches theoretical expectations.

Table 4.2: Experiment-2 Results

Load (No. of resistors)	Pressure (bar)	Voltage V (volts)	Current I (amps)	Speed (rpm)	Power V*I (watts)
No load	1	4.4	0	3940	0
	1.5	8.77	0	7890	0
	2	10.02	0	9080	0
1	1	3.38	0.66	3160	2.2308
	1.5	5.15	0.92	4780	4.738
	2	7.1	1.26	6680	8.946
	3	9.85	1.74	9850	17.139
2	1	2.36	0.77	2265	1.8172
	1.5	3.84	1.24	3690	4.7616
	2	5.07	1.64	4886	8.3148
	2.5	6.18	2.06	5945	12.7308
	2.75	6.75	2.23	6520	15.0525
	3	7.64	2.5	7444	19.1
	3.5	8.5	2.76	8300	23.46
	4	9.82	3.273	10200	32.1408
	6	13.2	4.4	14350	58.08
	8	15.9	5.3	16985	84.27
4	8.8	16.98	5.65	17500	95.937
	1	1.32	0.8	1320	1.056
	2	4	2.5	4000	10
	4	7.65	4.9	7960	37.485
	6	8.45	5.6	9640	47.32
	8	11.03	7.36	13200	81.1808
6	8.8	11.89	7.9	14300	93.931
	2	2.402	2.389	2760	5.7383
	4	4.85	4.82	5680	23.377
	6	6.42	6.39	7690	41.0238
	8	8.06	8.05	9862	64.883
8	8.8	8.98	9	11100	80.82
	3	2.87	3.8	3566	10.906
	5	6.06	4.57	5850	27.6942
	7	7.72	5.82	7612	44.9304
	8	8.48	6.39	8372	54.1872
	8.8	9.39	7.09	9465	66.5751

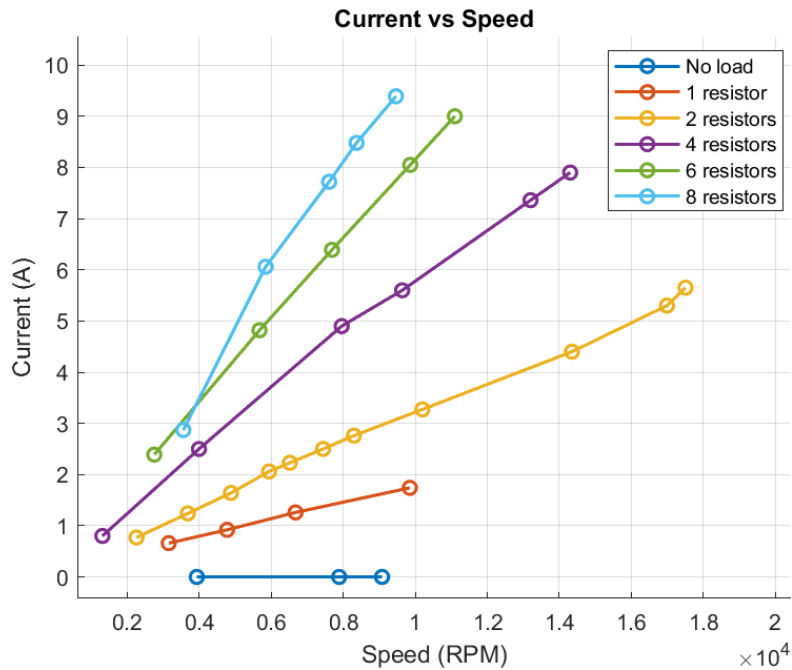


Figure 4.5 Current (Y) vs. Speed (X) for Experiment - 2

4.2 CFD Validation

A scatter contour plot of power versus pressure was generated for the second experiment, with the color of the data points representing the RPM. This plot visualizes the relationship between power and pressure across different operating conditions. The power versus pressure data from the laminar and turbulent CFD simulations of the Mark-1 turbine, incorporating the turbulence model, were superimposed on the experimental results. The CFD data was collected at inlet pressures of 2, 5, and 8 bar, with an outlet pressure of 1 bar, and at rotational speeds of 8000, and 16000 RPM, as shown in Figure 4.6.

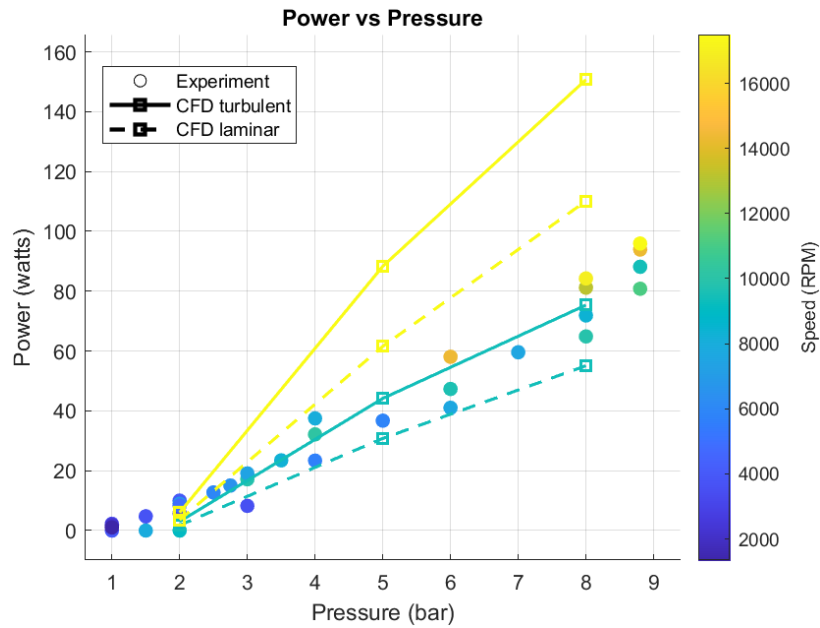


Figure 4.6 Power (Y) vs. Pressure (X) for Experiment and CFD (laminar and turbulent)

The comparison between the experimental and CFD results indicates that the CFD values align closely with the experimental data at lower speeds. However, at higher speeds, the discrepancies between the two sets of results become more pronounced. The laminar solution deviates by around 20%, which could be attributed to discrepancies in mass flow.

CHAPTER 5

Conclusions

This research has focused on the numerical assessment of a bladeless turbine with air as its working fluid. A mesh refinement of the nozzle slot between upstream nozzle and disk was conducted to determine the optimal number of cells to be used throughout the study to strike a balance between accuracy and computational cost. The numerical domain includes the stationary nozzle, nozzle-rotor gap and rotor, and resulted in a spiral flow path behavior, typical of Tesla turbines. Reynolds number contours were plotted to study the fluid behaviour and the flow was observed to be turbulent in the nozzle slot and at the entry of disk whereas laminar throughout the disk. Laminar solutions were plotted against the turbulent model solutions showing the torque in turbulent gains more compared to the laminar one with increase in RPM while the mass flow is nearly equal in both the cases. Turbine characteristics, total pressure ratio at inlet to outlet versus mass flow parameter as well as specific power were analyzed, and flow angles were used to identify the optimal range of the bladeless turbine for several pressure ratios. Finally, the boundary layer profiles upstream of the rotor were investigated. For a mass flows of $4.66\text{E-}04$ kg/s and radius of 75mm, powers up to 6.5 Watts were extracted.

Choking was observed in the fluid in the slot for all the inlet pressures. Two types of nozzle slot configurations were investigated, a flat and convergent-divergent (CD). Transitioning the configuration from flat to CD resulted in the improvement in the coefficient of discharge (Cd) by around 13%. Nozzle inclination angles from 15 to 75 degrees were studied and a nozzle inclination angle range of 45 to 50 degrees was found to be optimum. Multi nozzle cases with two, four, six and eight nozzles were studied. Increasing the pressure ratio in a two-nozzle configuration was found beneficial than increasing the number of nozzles.

Experiments were conducted with two different wattages generator to validate both laminar and turbulent flow CFD model. Power values were closely matching at lower RPMs but at higher RPMs, the discrepancies between the two sets of results become more pronounced. Laminar solutions were found to be deviating from experiment values by around 20%.

REFERENCES

- [1] N.Tesla, 1913, “Turbine,” US Patent 1061206.
- [2] N.Tesla,1913, “Fluid Propulsion,” US Patent 1061142.
- [3] V. D. Romanin, “Theory and Performance of Tesla Turbines,” 2012.
- [4] R. N. Tiwari, F. Reggio, M. L. Ferrari, W. De Paepe, and A. Traverso, “Experimental Characterization of a Bladeless,” 2024.
- [5] Cengel and Cimbala, “ Fluid Mechanics: Fundamentals and Applications,” 3rd edition, 2014.
- [6] Alberto Traverso, Avinash Renuke, Anestis I. Kalfas, “Tesla Turbine: A Practical Design Guide for Boundary Layer or Bladeless Turbines,” 2024.
- [7] Armstrong JH, “An investigation of the performance of a modified Tesla turbine.” PhD Thesis, Georgia Institute of Technology, USA, 1952.
- [8] W. Rice, “An Analytical and Experimental Investigation of Multiple Disk Turbines,” ASME J. Eng. Power, 87(1), pp. 29–36, 1965.
- [9] A. Guha, “Structure of partly dispersed normal shock waves in vapour-droplet flows,” Phys. Fluids A 4 (7) 1566–1578, 1992.
- [10] A. Guha, “Jump conditions across normal shock waves in pure vapour droplet flows,” J. Fluid Mech. 241 349–369, 1992.
- [11] A. Guha, “A unified theory for the interpretation of total pressure and temperature in two-phase flows at subsonic and supersonic speeds,” Proc. R. Soc. Lond. Ser.A Math. Phys. Eng. Sci. 454 671–695, 1998
- [12] “A. Guha, A unified theory of aerodynamic and condensation shock waves in vapour-droplet flows with or without a carrier gas,” Phys. Fluids A 6 (5), 1994.

- [13] A. Guha, “Computation, analysis and theory of two-phase flows,” *Aeronaut. J.*102 (1012) 71–82, 1998
- [14] A. G. G.P. Hoya, “The design of a test rig and study of the performance and efficiency of a Tesla disc turbine, *Proc. IMechE, Part A, J. Power and Energy* 223 (A4) 451–465,” 2009
- [15] Sengupta S, and Guha A, “Inflow-Rotor Interaction in Tesla Disc Turbines: Effect of Discrete Inflows, Finite Disk Thickness and the Radial Clearance on the Fluid Dynamics and the Performance of the Turbine,” *Proc. Inst.Mech. Eng., Part A*, 232(8), pp. 971–991, 2018.
- [16] W. Rice, “Tesla turbomachinery, in: E. Logan (Ed.), *Handbook of Turbomachinery*,” Marcel Dekker, New York, pp. 861–874, 2003.
- [17] B. E. , and R. W. Boyack, “Integral Method for Flow Between Corotating Disks,” *ASME J. Basic Eng.*, 93(3), pp. 350–354., 1971.
- [18] C. E. Bassett, “An Integral Solution for Compressible Flow Through Disc Turbines,” *Proceedings of the Tenth Intersociety Energy Conversion Engineering Conference*, Newark, Delaware, Aug. 17–22, pp. 1098–1106, 1975.
- [19] Leaman AB, “The design, construction and investigation of a Tesla turbine.” MS Thesis, University of Maryland, USA, 1950.
- [20] J.H. Armstrong, “An Investigation of the Performance of a Modified Tesla Turbine,” M.S. Thesis, Georgia Institute of Technology, 1952.
- [21] Beans EW, “Performance characteristics of a friction disc turbine.” PhD Thesis, Pennsylvania State University, USA, 1961.

- [22] North RC, “An investigation of the Tesla turbine.” PhD Thesis, University of Maryland, USA, 1969.
- [23] Ladino AFR, “Numerical simulation of the flow field in a friction-type turbine (Tesla turbine).” PhD Thesis, National University of Colombia, Colombia, 2004.
- [24] McGarey S and Monson P, “Performance and efficiency of disk turbines. MEng Research Project Report (Advisor: A Guha),” Report No. 1203, Aerospace Engineering Department, University of Bristol, UK, 2007.
- [25] Hoya GP, “Performance and efficiency of disk turbines. MEng Research Project Report (Advisor: A Guha),” Report No. 1277, Aerospace Engineering Department, University of Bristol, UK, 2008.
- [26] Smiley B, “Performance and efficiency of the nozzle in a Tesla disk turbine. MEng Research Project Report (Advisor: A Guha),” Report No. 1294, Aerospace Engineering Department, University of Bristol, UK, 2009.
- [27] G. , P. L. , and T. L. Manfrida, “An Upgraded Tesla Turbine Concept for ORC Applications,” *Energy*, Vol. 158, pp. 33-40,2018.
- [28] K. , and G. K. , Okamoto, ““Experimental Investigation of Inflow Condition Effects on Tesla Turbine Performance’, ISABE, International Symposium on Air Breathing Engine, pp. 1-11. ,” 2017.
- [29] A. , R. F. , F. M. , P. M. , and T. A. Renuke, “Experimental Characterization of Losses in Bladeless Turbine Prototype,ASME J. Eng. Gas Turbines Power, 144(4), p. 041009” ,2022.
- [30] V. Izraelev *et al.*, “A passively suspended tesla pump left ventricular assist device,” *ASAIO Journal*, vol. 55, no. 6, pp. 556–561, Nov. 2009.

- [31] C.-S. Jhun, R. Newswanger, J. Cysyk, B. Lukic, W. Weiss, and G. Rosenberg, “TESLA-BASED BLOOD PUMP AND ITS APPLICATIONS,” 2013.
- [32] L. Talluri, D. Fiaschi, G. Neri, and L. Ciappi, “Design and optimization of a Tesla turbine for ORC applications,” *Appl Energy*, vol. 226, pp. 300–319, Sep. 2018.
- [33] M. Ruiz and V. P. Carey, “Experimental study of single phase heat transfer and pressure loss in a spiraling radial inflow microchannel heat sink,” *J Heat Transfer*, vol. 137, no. 7, Jul. 2015.
- [34] N. Patel and D. D. Schmidt, “Biomass Boundary Layer Turbine Power System,” 2002.
- [35] M. Passalacqua, S. Maccarini, and A. Traverso, “CO₂ reverse cycles equipped with a bladeless turboexpander,” *Energy Convers Manag*, vol. 293, Oct. 2023.